

## Euclid Quick Data Release (Q1)

### The Strong Lensing Discovery Engine C – Finding lenses with machine learning

Euclid Collaboration: N. E. P. Lines<sup>1</sup>, T. E. Collett<sup>1</sup>, M. Walmsley<sup>2,3</sup>, K. Rojas<sup>4,1</sup>, T. Li<sup>1</sup>, L. Leuzzi<sup>5,6</sup>, A. Manjón-García<sup>7</sup>, S. H. Vincken<sup>4</sup>, J. Wilde<sup>8</sup>, P. Holloway<sup>9</sup>, A. Verma<sup>9</sup>, R. B. Metcalf<sup>5,6</sup>, I. T. Andika<sup>10,11</sup>, A. Melo<sup>11,10</sup>, M. Melchior<sup>4</sup>, H. Domínguez Sánchez<sup>12</sup>, A. Díaz-Sánchez<sup>7</sup>, J. A. Acevedo Barroso<sup>13</sup>, B. Clément<sup>13,14</sup>, C. Krawczyk<sup>1</sup>, R. Pearce-Casey<sup>15</sup>, S. Serjeant<sup>15</sup>, F. Courbin<sup>8,16</sup>, G. Despali<sup>5,6,17</sup>, R. Gavazzi<sup>18,19</sup>, S. Schuldt<sup>20,21</sup>, H. Degaudenzi<sup>22</sup>, L. R. Ecker<sup>23,24</sup>, W. J. R. Enzi<sup>1</sup>, K. Finner<sup>25</sup>, A. Galan<sup>10,11</sup>, C. Giocoli<sup>6,17</sup>, N. B. Hogg<sup>26</sup>, K. Jahnke<sup>27</sup>, S. Kruk<sup>28</sup>, G. Mahler<sup>29,30,31</sup>, A. More<sup>32,33</sup>, B. C. Nagam<sup>34,35</sup>, J. Pearson<sup>15</sup>, A. Sainz de Murieta<sup>1</sup>, C. Scarlata<sup>34</sup>, D. Sluse<sup>29</sup>, A. Sonnenfeld<sup>36</sup>, C. Spiniello<sup>9</sup>, T. T. Thai<sup>18,37</sup>, C. Tortora<sup>38</sup>, L. Ulivi<sup>39,40,41</sup>, L. Weisenbach<sup>1</sup>, M. Zumalacarregui<sup>42</sup>, N. Aghanim<sup>43</sup>, B. Altieri<sup>28</sup>, A. Amara<sup>44</sup>, S. Andreon<sup>45</sup>, N. Auricchio<sup>6</sup>, H. Aussel<sup>46</sup>, C. Baccigalupi<sup>47,48,49,50</sup>, M. Baldi<sup>51,6,17</sup>, A. Balestra<sup>52</sup>, S. Bardelli<sup>6</sup>, P. Battaglia<sup>6</sup>, R. Bender<sup>24,23</sup>, F. Bernardeau<sup>53,19</sup>, A. Biviano<sup>48,47</sup>, A. Bonchi<sup>54</sup>, D. Bonino<sup>55</sup>, E. Branchini<sup>56,57,45</sup>, M. Brescia<sup>58,38</sup>, J. Brinchmann<sup>59,60</sup>, S. Camera<sup>61,62,55</sup>, G. Cañas-Herrera<sup>63,64,65</sup>, V. Capobianco<sup>55</sup>, C. Carbone<sup>21</sup>, V. F. Cardone<sup>66,67</sup>, J. Carretero<sup>68,69</sup>, S. Casas<sup>70</sup>, M. Castellano<sup>66</sup>, G. Castignani<sup>6</sup>, S. Cavuoti<sup>38,71</sup>, K. C. Chambers<sup>72</sup>, A. Cimatti<sup>73</sup>, C. Colodro-Conde<sup>74</sup>, G. Congedo<sup>75</sup>, C. J. Conselice<sup>3</sup>, L. Conversi<sup>76,28</sup>, Y. Copin<sup>77</sup>, A. Costille<sup>18</sup>, H. M. Courtois<sup>78</sup>, M. Cropper<sup>79</sup>, A. Da Silva<sup>80,81</sup>, G. De Lucia<sup>48</sup>, A. M. Di Giorgio<sup>82</sup>, C. Dolding<sup>79</sup>, H. Dole<sup>43</sup>, F. Dubath<sup>22</sup>, C. A. J. Duncan<sup>3</sup>, X. Dupac<sup>28</sup>, S. Escoffier<sup>83</sup>, M. Fabricius<sup>24,23</sup>, M. Farina<sup>82</sup>, R. Farinelli<sup>6</sup>, F. Faustini<sup>54,66</sup>, S. Ferriol<sup>77</sup>, F. Finelli<sup>6,84</sup>, S. Fotopoulou<sup>85</sup>, M. Frailis<sup>48</sup>, E. Franceschi<sup>6</sup>, M. Fumana<sup>21</sup>, S. Galeotta<sup>48</sup>, K. George<sup>23</sup>, W. Gillard<sup>83</sup>, B. Gillis<sup>75</sup>, P. Gómez-Alvarez<sup>86,28</sup>, J. Gracia-Carpio<sup>24</sup>, B. R. Granett<sup>45</sup>, A. Grazian<sup>52</sup>, F. Grupp<sup>24,23</sup>, L. Guzzo<sup>20,45,87</sup>, S. Gwyn<sup>88</sup>, S. V. H. Haugan<sup>89</sup>, W. Holmes<sup>90</sup>, I. M. Hook<sup>91</sup>, F. Hormuth<sup>92</sup>, A. Hornstrup<sup>93,94</sup>, P. Hudelot<sup>19</sup>, M. Jhabvala<sup>95</sup>, E. Keihänen<sup>96</sup>, S. Kermiche<sup>83</sup>, A. Kiessling<sup>90</sup>, B. Kubik<sup>77</sup>, M. Kümmel<sup>23</sup>, M. Kunz<sup>97</sup>, H. Kurki-Suonio<sup>98,99</sup>, Q. Le Boulc'h<sup>100</sup>, A. M. C. Le Brun<sup>101</sup>, D. Le Mignant<sup>18</sup>, S. Ligori<sup>55</sup>, P. B. Lilje<sup>89</sup>, V. Lindholm<sup>98,99</sup>, I. Lloro<sup>102</sup>, G. Mainetti<sup>100</sup>, D. Maino<sup>20,21,87</sup>, E. Maiorano<sup>6</sup>, O. Mansutti<sup>48</sup>, S. Marcin<sup>103</sup>, O. Marggraf<sup>104</sup>, M. Martinelli<sup>66,67</sup>, N. Martinet<sup>18</sup>, F. Marulli<sup>5,6,17</sup>, R. Massey<sup>31</sup>, S. Maurogordato<sup>105</sup>, E. Medinaceli<sup>6</sup>, S. Mei<sup>106,107</sup>, Y. Mellier<sup>108,19</sup>, M. Meneghetti<sup>6,17</sup>, E. Merlin<sup>66</sup>, G. Meylan<sup>13</sup>, A. Mora<sup>109</sup>, M. Moresco<sup>5,6</sup>, L. Moscardini<sup>5,6,17</sup>, R. Nakajima<sup>104</sup>, C. Neissner<sup>110,69</sup>, R. C. Nichol<sup>44</sup>, S.-M. Niemi<sup>63</sup>, J. W. Nightingale<sup>111</sup>, C. Padilla<sup>110</sup>, S. Paltani<sup>22</sup>, F. Pasian<sup>48</sup>, K. Pedersen<sup>112</sup>, W. J. Percival<sup>113,114,115</sup>, V. Pettorino<sup>63</sup>, S. Pires<sup>46</sup>, G. Polenta<sup>54</sup>, M. Poncet<sup>116</sup>, L. A. Popa<sup>117</sup>, L. Pozzetti<sup>6</sup>, F. Raison<sup>24</sup>, R. Rebolo<sup>74,118,119</sup>, A. Renzi<sup>120,121</sup>, J. Rhodes<sup>90</sup>, G. Riccio<sup>38</sup>, E. Romelli<sup>48</sup>, M. Roncarelli<sup>6</sup>, R. Saglia<sup>23,24</sup>, Z. Sakr<sup>122,123,124</sup>, A. G. Sánchez<sup>24</sup>, D. Sapone<sup>125</sup>, B. Sartoris<sup>23,48</sup>, J. A. Schewtschenko<sup>75</sup>, M. Schirmer<sup>27</sup>, P. Schneider<sup>104</sup>, T. Schrabback<sup>126</sup>, A. Secroun<sup>83</sup>, G. Seidel<sup>27</sup>, M. Seiffert<sup>90</sup>, S. Serrano<sup>127,128,129</sup>, P. Simon<sup>104</sup>, C. Sirignano<sup>120,121</sup>, G. Sirri<sup>17</sup>, A. Spurio Mancini<sup>130</sup>, L. Stanco<sup>121</sup>, J. Steinwagner<sup>24</sup>, P. Tallada-Crespí<sup>68,69</sup>, A. N. Taylor<sup>75</sup>, I. Tereno<sup>80,131</sup>, S. Toft<sup>132,133</sup>, R. Toledo-Moreo<sup>134</sup>, F. Torradeflot<sup>69,68</sup>, I. Tutusaus<sup>123</sup>, E. A. Valentijn<sup>35</sup>, L. Valenziano<sup>6,84</sup>, J. Valiviita<sup>98,99</sup>, T. Vassallo<sup>23,48</sup>, G. Verdoes Kleijn<sup>35</sup>, A. Veropalumbo<sup>45,57,56</sup>, Y. Wang<sup>135</sup>, J. Weller<sup>23,24</sup>, A. Zacchei<sup>48,47</sup>, G. Zamorani<sup>6</sup>, F. M. Zerbi<sup>45</sup>, E. Zucca<sup>6</sup>, V. Allevato<sup>38</sup>, M. Ballardini<sup>136,137,6</sup>, M. Bolzonella<sup>6</sup>, E. Bozzo<sup>22</sup>, C. Burigana<sup>138,84</sup>, R. Cabanac<sup>123</sup>, A. Cappi<sup>6,105</sup>, D. Di Ferdinando<sup>17</sup>, J. A. Escartin Vigo<sup>24</sup>, L. Gabarra<sup>9</sup>, J. Martín-Fleitas<sup>109</sup>, S. Matthew<sup>75</sup>, N. Mauri<sup>73,17</sup>, A. Pezzotta<sup>139,24</sup>, M. Pöntinen<sup>98</sup>, C. Porciani<sup>104</sup>, I. Risso<sup>140</sup>, V. Scottez<sup>108,141</sup>, M. Sereno<sup>6,17</sup>, M. Tenti<sup>17</sup>, M. Viel<sup>47,48,50,49,142</sup>, M. Wiesmann<sup>89</sup>, Y. Akrami<sup>143,144</sup>, S. Anselmi<sup>121,120,145</sup>, M. Archidiacono<sup>20,87</sup>, F. Atrio-Barandela<sup>146</sup>, C. Benoist<sup>105</sup>, K. Benson<sup>79</sup>, P. Bergamini<sup>20,6</sup>, D. Bertacca<sup>120,52,121</sup>, M. Bethermin<sup>147</sup>, A. Blanchard<sup>123</sup>, L. Blot<sup>148,145</sup>, M. L. Brown<sup>3</sup>, S. Bruton<sup>149</sup>, A. Calabro<sup>66</sup>, F. Caro<sup>66</sup>, C. S. Carvalho<sup>131</sup>, T. Castro<sup>48,49,47,142</sup>, Y. Charles<sup>18</sup>, F. Cogato<sup>5,6</sup>, A. R. Cooray<sup>150</sup>, O. Cucciati<sup>6</sup>, S. Davini<sup>57</sup>, F. De Paolis<sup>151,152,153</sup>, G. Desprez<sup>35</sup>, J. J. Diaz<sup>154</sup>, S. Di Domizio<sup>56,57</sup>, J. M. Diego<sup>12</sup>, A. Enia<sup>51,6</sup>, Y. Fang<sup>23</sup>, A. G. Ferrari<sup>17</sup>, A. Finoguenov<sup>98</sup>, A. Fontana<sup>66</sup>, A. Franco<sup>152,151,153</sup>, K. Ganga<sup>106</sup>, J. García-Bellido<sup>143</sup>, T. Gasparetto<sup>48</sup>, V. Gautard<sup>155</sup>, E. Gaztanaga<sup>129,127,1</sup>, F. Giacomini<sup>17</sup>, F. Gianotti<sup>6</sup>, G. Gozaliasl<sup>156,98</sup>, M. Guidi<sup>51,6</sup>, C. M. Gutierrez<sup>157</sup>, A. Hall<sup>75</sup>, W. G. Hartley<sup>22</sup>, C. Hernández-Monteagudo<sup>119,74</sup>, H. Hildebrandt<sup>158</sup>, J. Hjorth<sup>112</sup>,

J. J. E. Kajava<sup>159, 160</sup>, Y. Kang<sup>22</sup>, V. Kansal<sup>161, 162</sup>, D. Karagiannis<sup>136, 163</sup>, K. Kiiveri<sup>96</sup>, C. C. Kirkpatrick<sup>96</sup>, J. Le Graet<sup>83</sup>, L. Legrand<sup>164, 165</sup>, M. Lembo<sup>136, 137</sup>, F. Lepori<sup>166</sup>, G. Leroy<sup>30, 31</sup>, G. F. Lesci<sup>5, 6</sup>, J. Lesgourgues<sup>70</sup>, T. I. Liaudat<sup>167</sup>, S. J. Liu<sup>82</sup>, A. Loureiro<sup>168, 169</sup>, J. Macias-Perez<sup>170</sup>, G. Maggio<sup>48</sup>, M. Magliocchetti<sup>82</sup>, E. A. Magnier<sup>72</sup>, F. Mannucci<sup>41</sup>, R. Maoli<sup>171, 66</sup>, C. J. A. P. Martins<sup>172, 59</sup>, L. Maurin<sup>43</sup>, M. Miluzio<sup>28, 173</sup>, P. Monaco<sup>174, 48, 49, 47</sup>, C. Moretti<sup>50, 142, 48, 47, 49</sup>, G. Morgante<sup>6</sup>, S. Nadathur<sup>1</sup>, K. Naidoo<sup>1</sup>, A. Navarro-Alsina<sup>104</sup>, S. Nesseris<sup>143</sup>, F. Passalacqua<sup>120, 121</sup>, K. Paterson<sup>27</sup>, L. Patrizii<sup>17</sup>, A. Pisani<sup>83, 175</sup>, D. Potter<sup>166</sup>, S. Quai<sup>5, 6</sup>, M. Radovich<sup>52</sup>, P.-F. Rocci<sup>43</sup>, S. Sacquegna<sup>151, 152, 153</sup>, M. Sahlén<sup>176</sup>, D. B. Sanders<sup>72</sup>, E. Sarpa<sup>50, 142, 49</sup>, A. Schneider<sup>166</sup>, D. Sciotti<sup>66, 67</sup>, E. Sellentin<sup>177, 65</sup>, L. C. Smith<sup>178</sup>, K. Tanidis<sup>9</sup>, G. Testera<sup>57</sup>, R. Teyssier<sup>175</sup>, S. Tosi<sup>56, 57, 45</sup>, A. Troja<sup>120, 121</sup>, M. Tucci<sup>22</sup>, C. Valieri<sup>17</sup>, A. Venhola<sup>179</sup>, D. Vergani<sup>6</sup>, G. Vernardos<sup>180, 181</sup>, G. Verza<sup>182</sup>, P. Vielzeuf<sup>83</sup>, N. A. Walton<sup>178</sup>, and D. Scott<sup>183</sup>

(Affiliations can be found after the references)

March 20, 2025

## ABSTRACT

Strong gravitational lensing has the potential to provide a powerful probe of astrophysics and cosmology, but fewer than 1000 strong lenses have been confirmed previously. With  $0''.16$  resolution covering a third of the sky, the *Euclid* telescope will revolutionise strong lens finding, with 170 000 lenses forecasted to be discovered amongst its 1.5 billion galaxies. We present an analysis of the performance of five machine-learning models at finding strong gravitational lenses in the quick release of *Euclid* data (Q1), covering  $63 \text{ deg}^2$ . The models are validated with citizen scientists and expert visual inspection. We focus on the best performing network: a fine-tuned version of the Zoobot pretrained model, originally trained to classify galaxy morphologies in heterogeneous astronomical imaging surveys. Of the one million Q1 objects that Zoobot was tasked to find strong lenses within, the top 1000 ranked objects contained 122 grade A lenses (almost certain lenses), and 41 grade B lenses (probable lenses). A deeper search with the five networks combined with visual inspection discovered 250 (247) grade A (B) lenses, of which 224 (182) are ranked in the top 20 000 by Zoobot. When extrapolated to the full *Euclid* survey, the highest ranked one million images will contain 75 000 grade A or B strong gravitational lenses.

**Key words.** Gravitational lensing: strong – Catalogs – Surveys

## 1. Introduction

Covering approximately  $14\,000 \text{ deg}^2$ , the Euclid Wide Survey (EWS; [Euclid Collaboration: Mellier et al. 2024](#)) has the power to revolutionise strong gravitational lensing by galaxies, transforming it from a sample of about a thousand to over a hundred thousand ([Collett 2015](#)). Whilst many telescopes on the ground have surveyed large areas of sky, no previous wide area survey has ever had sufficient resolution to resolve multiple images of a single background source around a typical lens galaxy. The Einstein radius distribution of galaxy-galaxy lenses in the Universe is expected to peak at  $0''.4$  ([Collett 2015](#)), and many of these are within reach of *Euclid* with the  $0''.16$  full width at half maximum (FWHM) in the VIS filter ([Euclid Collaboration: McCracken et al. 2025](#)).

With exceptional resolution comes exceptional challenges of data volume. *Euclid* will observe around 1.5 billion unlensed galaxies ([Euclid Collaboration: Scaramella et al. 2022](#)) in its  $14\,000 \text{ deg}^2$ , and manually searching these is intractable. Even the largest citizen science lens search projects have only inspected up to around one million images ([Marshall et al. 2015](#); [More et al. 2016](#); [Sonnenfeld et al. 2020](#); [González et al. 2025](#)). To deliver the promise of *Euclid* strong lens finding, it is clear that automated methods must be employed to pre-screen candidates.

Recently, machine learning has gained substantial traction in the field of strong lens finding, with many teams developing machine-learning-based classifiers ([Metcalfe et al. 2019](#)). [Lanusse et al. \(2018\)](#) and [Avestruz et al. \(2019\)](#) developed deep convolutional neural network (CNN) architectures that performed extremely well on simulated lenses ([Metcalfe et al. 2019](#)),

whilst [Jacobs et al. \(2017\)](#) trained a CNN to find 14 lens candidates per square degree in the Canada–France–Hawaii Telescope (CFHT) data. CNNs have now been successfully employed to find lenses in the Dark Energy Survey (DES, [Jacobs et al. 2019b,a](#); [Rojas et al. 2022](#)), the Kilo-Degree Survey (KiDS, [Petrillo et al. 2017, 2019](#); [Li et al. 2020, 2021](#); [Nagam et al. 2023, 2024](#); [Grespan et al. 2024](#)), Panoramic Survey Telescope and Rapid Response System (PanSTARRS, [Cañameras et al. 2020](#)), the Ultraviolet Near-Infrared Optical Northern Survey (UNIONS, [Savary et al. 2022](#)), and Hyper Suprime-Cam (HSC) data ([Shu et al. 2022](#); [Jaelani et al. 2024](#)). More recently [González et al. \(2025\)](#) showed that multi-class vision transformers are powerful alternatives to CNNs.

Machine-learning approaches to strong lens finding are data intensive, requiring large samples of positive and negative example sets. Negative training sets are relatively easy to construct, since almost all astronomical objects are not strongly lensed. Constructing a positive training set is much more challenging, since the known lens sample is small and the observations heterogeneous. Faced with this problem, almost all strong lens finders have relied on simulations of lenses to act as positive training sets, using either pure simulations or lensed sources painted on top of real non-lensing luminous red galaxies (LRGs). These approaches allow for the creation of very large positive training sets, but carry a substantial risk that the machine-learning models may only learn peculiarities from the simulation process, rather than the true features that distinguish a lens from a non-lens.

The Euclid Quick Data Release 1 (Q1; [Euclid Quick Release Q1 2025](#)) data set gives the first opportunity to search for lenses in a large area ( $63 \text{ deg}^2$ ) homogeneous data set with  $0''.16$  resolution. Prior to this, the only *Euclid* data available for finding lenses within has been the *Euclid* Early Release Obser-

\* e-mail: natalie.lines@port.ac.uk

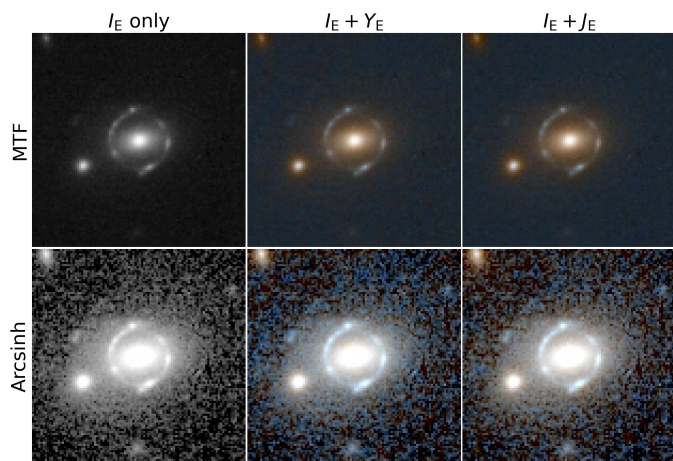


**Fig. 1.** Different scaling and colour options for one sample cutout in Q1 processed into JPEG format. The top row is MTF scaling and the bottom row is arcsinh scaling. From left to right, the columns show  $I_E$ -only,  $I_E + Y_E$ , and  $I_E + J_E$  images. The cutout size is  $100 \times 100$  pixels, or  $10'' \times 10''$  angular scale.

variations (ERO, [Euclid Early Release Observations 2024](#)) data, which covered an area of  $8.12 \text{ deg}^2$ . With these data, an area of  $0.7 \text{ deg}^2$  was entirely visually inspected down to  $I_E = 22.5$  by experts where three grade A and 13 grade B lens candidates were found ([Acevedo Barroso et al. 2024b](#)). These lenses were used to test machine-learning models at finding lenses in *Euclid* ([Pearce-Casey et al. 2024](#)), and these models were then applied to the rest of the ERO, data where 14 grade A and 31 grade B strong lens candidates were found ([Nagam et al. 2025](#)).

This paper describes the efforts within the Euclid Consortium to train machine-learning models to discover strong lenses in Q1, which is part of the five paper series ‘The Strong Lensing Discovery Engine’. The series consists of: the overview paper [Euclid Collaboration: Walmsley et al. \(2025\)](#) that includes a description of all the lenses found in Q1; [Euclid Collaboration: Rojas et al. \(2025\)](#) that describes our effort to build a strong lens training set for Q1; this paper that describes the machine-learning lens finding effort; [Euclid Collaboration: Li et al. \(2025\)](#) that analyses the double-source-plane lens (DSPL) candidates that were discovered; and [Euclid Collaboration: Holloway et al. \(2025\)](#) that explores how to combine multiple lens-finding classifiers into an ensemble classifier for future lens searches.

The present paper is structured as follows. In Sect. 2 we discuss the data used in this work, which consists of the *Euclid* Q1 data (Sect. 2.1) and the machine-learning training data (Sect. 2.2). In Sect. 3 we describe the Zoobot machine-learning model and present what was learnt from optimising Zoobot to find lenses. In Sect. 4 we explore the other machine-learning models used in this work. The results are presented in Sect. 5, which include the results from a preliminary inspection of each model’s top 1000 ranked objects (Sect. 5.1), the results from combining machine learning with citizen science to find lenses in Q1 (Sect. 5.2), and a statistical analysis of how many lenses there are in Q1 beyond what was visually inspected (Sect. 5.3). A discussion of what was found is presented in Sect. 6 and the conclusions are presented in Sect. 7.

## 2. Data

*Euclid* collects data with two instruments, the visible imager (VIS; [Euclid Collaboration: Cropper et al. 2024](#)) and the near-

infrared spectrometer and photometer (NISP; [Euclid Collaboration: Jahnke et al. 2024](#)). There are four bands in total, the VIS  $I_E$  band and the NISP  $Y_E$ ,  $J_E$ , and  $H_E$  bands. Although *Euclid* images are originally in FITS (Flexible Image Transport System) format, the quantity of data meant that it was necessary to work with JPEG (Joint Photographic Experts Group) files, which required a choice of scaling and filters. Three choices of filter combinations with two image scalings were chosen, producing a total of six combinations. The filter combinations used were  $I_E$ -only greyscale images,  $I_E + Y_E$  colour images, and  $I_E + J_E$  colour images. In the case of the colour images, the red/blue channels correspond to the longest/shortest wavelength images, and the green channel is the median of the two. All images are produced at the highest resolution of the *Euclid* bands, that of VIS  $I_E$ , at  $0''.101$  per pixel (see [Euclid Collaboration: Walmsley et al. 2025](#) for details). The two scalings chosen were arcsinh, which provides a high contrast that amplifies both faint arcs and background noise, and the midtone-transfer function (MTF; see [Euclid Collaboration: Walmsley et al. 2025](#)), which produces a more homogenous image without saturating bright pixels. An example of these images for one cutout is shown in Fig. 1. Although converting images from FITS to JPEG files necessarily means some information is lost, the full 16 bits of information per pixel in FITS files results in large quantities of mostly redundant information. Providing that the scaling to the 8-bit format of JPEG images is such that it preserves most of the dynamic range, the amount of information lost is made up for by the significantly faster processing time. We find that for both the brightest and the faintest of lenses (whether these be the lenses we find in Q1 or lenses found in previous searches), the lenses are generally as easy to distinguish in the JPEG images as in the FITS images. These options were chosen based on the appearance of the Q1 data, but the same scalings were applied to simulations and other training and validation data to ensure homogeneity. All images have a size of  $100 \times 100$  pixels, corresponding to an angular scale of  $10'' \times 10''$  in the  $I_E$  band. This size allows the full Einstein ring of all galaxy-scale lenses to be visible but does not necessarily encompass group-scale lenses.

### 2.1. Q1 data

*Euclid* collects data for two main surveys: the EWS and the Euclid Deep Survey (EDS). The former aims to survey around a third of the sky, covering the area that excludes the Galactic and ecliptic plane, amounting to  $14\,000 \text{ deg}^2$ , while the latter surveys three selected areas (Euclid Deep Field North, Euclid Deep Field South, and Euclid Deep Field Fornax), totalling  $63 \text{ deg}^2$ , but with repeated exposures producing images that are up to 2 magnitudes deeper. The *Euclid* Q1 release covers the Deep Field areas, but at the depth of the EWS. Q1 provides the first look into what we will be able to find within *Euclid*’s lifetime and provides us with the first sample of *Euclid* lenses.

The *Euclid* data products we used were the background-subtracted merged mosaic tiles, in which the four images from the different *Euclid* bands are matched to the resolution of VIS  $I_E$ . While  $I_E$  has a PSF FWHM of  $0''.16$  ([Euclid Collaboration: Cropper et al. 2024](#)), for  $Y_E$ ,  $J_E$ , and  $H_E$  the PSF FWHM is  $0''.35$ ,  $0''.34$ , and  $0''.35$ , respectively ([Euclid Collaboration: Jahnke et al. 2024](#)), and the details of the interpolation are described in [Euclid Collaboration: Romelli et al. \(2025\)](#). Of all the objects in Q1, 1 086 554 passed our selection criteria of  $I_E < 22.5$ , along with a quality check to remove objects such as stars (see [Euclid Collaboration: Walmsley et al. 2025](#)), and it was these objects that were analysed by the machine-learning models. Using cutouts

with size  $10'' \times 10''$  means there will inevitably be overlap between images, but we ensure that the numbers of lenses reported has duplicate lenses removed.

## 2.2. Training and validation data sets

For the Q1 lens finding challenge, any member of the Euclid Collaboration strong lensing working group was invited to develop a machine-learning model. Many of the models used in this work were built on models developed for the strong lens search in the *Euclid* ERO data (Acevedo Barroso et al. 2024b; Pearce-Casey et al. 2024; Nagam et al. 2025), which were the first investigations of the lens-finding ability of *Euclid*. Given the aim of finding as many lenses as possible, there were few restrictions placed on how the models should be developed; rather, they were all developed independently and evaluated on their Q1 lens-finding performance.

Machine-learning models are best able to recognise images that appear similar to the images they have been trained on, meaning ideally we want to train the models on real *Euclid* lenses. However, the number of objects needed to train deep learning models (typically of the order  $10^4$ – $10^5$ ) greatly exceeds the number of known lenses. While pretrained models can greatly reduce the number of images that are needed to be trained on (of the order  $10^3$ ), the number of available lenses is still too low to span the range of plausible strong lensing configurations. Therefore, we have to augment our set of known lenses with simulations on which to train the machine-learning models, which are then applied to the Q1 data.

At the time of training the machine-learning models in preparation for Q1, there were multiple options of what images to use. The different data sets available consisted of simulated lenses, known real lenses, and non-lenses. The different machine-learning models were developed independently and as such were free to choose any available data sets for training and validation of the models. All of these data sets were available as JPEG files in all of the six combinations of scalings and filters, and it was left to the developers of each model to choose which of these to use for their final model. By allowing a diversity of options in terms of choice of training data and image processing, we are more likely to be able to find an optimal approach for lens finding in future *Euclid* data releases, allowing us to later refine these options to be able to make more direct comparisons between models. In the future when a large number of real *Euclid* lenses are available, we will be able to quantify different machine-learning approaches in a fully data-driven way.

### 2.2.1. Simulated lenses

The first set of simulations (S1) was based on the work presented in Euclid Collaboration: Rojas et al. (2025) and was created as follows. They simulated strong lensing systems using all four *Euclid* bands, following the procedure outlined in Rojas et al. (2022) and utilising the Lenstronomy package (Birrer & Amara 2018; Birrer et al. 2021). Deflectors were selected as LRGs with known redshifts and velocity dispersions, modelled using a Sérsic profile in the  $J_e$  band to estimate ellipticities and central positions. These parameters were optimised with a downhill simplex algorithm. Background sources were drawn from the Hubble Space Telescope Advanced Camera for Surveys (ACS) F814W high-resolution catalogue (Leauthaud et al. 2007; Scoville et al. 2007; Koekemoer et al. 2007), combined with HSC colour information (Cañameras et al. 2020). VIS magnitudes were computed

by combining  $r$ -band +  $i$ -band images, while infrared magnitudes were matched to COSMOS 2020 VISTA (Visible and Infrared Survey Telescope for Astronomy)  $YJH$  bands (Weaver et al. 2022). They paired lenses and sources, such that they produce an Einstein radius in the range  $0''.5$ – $2''.0$ . A singular isothermal ellipsoid (SIE) mass model was adopted, with parameters derived from the Sérsic fit and Einstein radii calculated using the redshifts and velocity dispersions of the lens and source. Source images were lensed based on the mass model, and then down-sampled to match *Euclid* VIS  $I_e$  image resolution. This last step includes convolution with the telescope point-spread function (PSF) and scaling to the lens image flux. Finally, the resulting simulated lensing features are added into the VIS and NISP lens images. Through augmenting the number of LRGs available for simulating by using four  $90^\circ$  rotations of each LRG, the number of simulations was 11 057. There was an additional earlier version of the same simulations containing 10 311 simulations, making a total number of 21 368 simulations available.

A second set of simulations (S2) was created using the GLAMER lensing code (Metcalf & Petkova 2014; Petkova et al. 2014). These simulations started by cutting out  $200 \times 200$  pixel images of all the observed galaxies with  $I_e < 22$ . Each image was matched to an object in the Flagship simulation (Euclid Collaboration: Castander et al. 2024) with a nearest neighbour algorithm in the space of all magnitudes in all four bands, ellipticity, and redshift, when available for the observed galaxy. The parameters of the Flagship galaxy and dark matter halo were then used to construct a mass model for the lens. The mass model consisted of a baryonic part in the form of a Sérsic profile and a dark matter halo in the form of a Navarro–Frenk–White profile (Navarro et al. 1997). The position angle was set to that measured in the data. A source redshift was drawn from a distribution fit to the COSMOS 2020 FARMER catalogue  $I$ -band number counts (Weaver et al. 2022). Rays were then shot through the mass profile to the source redshift. The caustics and critical curves were found. The lens was rejected if the Einstein radius was less than  $0''.5$ . The Einstein radius is defined as the radius of a circle that has the same area as the area within the tangential critical curve. A source was then selected and placed near or in the tangential caustic. The sources were modelled with multiple Sérsic profiles. The image of the lensed object was then convolved with the local PSF, and Poisson noise was added. The simulations were performed at  $4\times$  the resolution of VIS  $I_e$ , then downsampled to the respective resolutions for VIS and NISP before being convolved with the PSFs. The NISP images were then interpolated to the higher VIS  $I_e$  resolution using a BILINEAR interpolation kernel, similar to the processing of the real *Euclid* data. Another rejection step was taken after combining the lensed image with the original data image. Cases where the lensed image was too low in signal-to-noise or in contrast to the lens galaxy light were removed when visually inspecting the images. In these simulations, the mass of neighbouring objects was not included. See Metcalf et al. (2025, in prep.) for more details on these and related simulations. 5363 images were created without any augmentation.

A third set of  $I_e$ -only simulations (S3) was created, implementing the code presented by Schuldt et al. (2021). To create galaxy-scale lens simulations, a lens mass distribution modelled with an SIE profile was used, with the following input parameters: lens redshift, source redshift, and velocity dispersion. The lens centroid, axis ratio, and position angle were derived from the first and second brightness moments of the *Euclid* VIS images. Sources were randomly placed in the source plane, restricting the simulations to those with an Einstein radius between  $0''.5$

and 2''5. Subsequently, the sources were lensed in the image plane using the GLEE software (Suyu & Halkola 2010; Suyu et al. 2012). Finally, the simulated lensed source image was convolved with the *Euclid* PSF, rescaled according to *Euclid*'s zero points, and combined with the original LRG image. The final simulations were given as images of 19'' $\times$  19'', with 2143 simulations produced.<sup>1</sup>

All of the simulations used for training employed painting simulated lensed sources on to real galaxies, as opposed to a fully simulated approach. We used three sets of simulations to increase training diversity. Two (S1 and S3) painted lensed sources on to galaxies with spectroscopically measured velocity dispersions, improving realism at the cost of using only bright LRGs as lenses (Euclid Collaboration: Rojas et al. 2025, Melo et al. in prep.). As high velocity dispersion LRGs were selected for this, the resulting simulations had disproportionately large Einstein radii, which could potentially bias the machine-learning models towards more massive lenses which are generally easier to detect. The other simulation set (S2) used proxies to avoid using spectra, resulting in potentially less physically realistic simulations but meaning that a much larger number of simulations could be produced around a wider range of galaxy types and masses (Metcalf 2025 in prep.). Only S1 and S2 produced simulations in the NISP bands. S1 produced the NISP images directly at the higher VIS  $I_E$  resolution, while S2 produced the NISP simulations at the lower resolution and then interpolated this to the resolution of VIS  $I_E$ , taking into account the correlated noise that exists in the real *Euclid* NISP images.

## 2.2.2. Previously known real lenses

Prior to this lens search, there were a number of previously known lenses coinciding with areas of *Euclid* coverage, which were ideal for training on as they most closely resemble the lenses in Q1. A data set of approximately 150 previously known grade A and B lenses that had Q1 data available was used in training and/or validation of the machine-learning models, but was not counted in the number of newly discovered lenses reported in this paper. This collection of 150 lenses includes lenses discovered in the *Euclid* ERO data (Acevedo Barroso et al. 2024b), the expert visual inspection of galaxies with spectroscopic velocity dispersion (Euclid Collaboration: Rojas et al. 2025), the Galaxy Zoo Cosmic Dawn project, other surveys that overlapped with Q1, and other serendipitous discoveries. Outside Q1, there were around 50 additional known grade A/B lenses in *Euclid* discovered from the Galaxy Zoo *Euclid* project, where volunteers searched the EWS, giving a total number of approximately 200 real *Euclid* lenses available for training. Around the time of the internal Q1 release, more lenses were discovered serendipitously, which were not discovered in time to add to our training sample, but which are collated in the Q1 lens data set presented in Euclid Collaboration: Walmsley et al. (2025).

As the number of known lenses is small and heterogeneous due to the number of different searches they originate from, training on these few known lenses alone may amplify any selection bias in the pre-existing lens sets. Therefore, these lenses were primarily used to supplement the simulated lenses, which are designed to cover a larger range of lensing configurations. Some machine-learning models were trained on the combina-

<sup>1</sup> We note that due to the nature of the internal Euclid Collaboration Q1 timeline, this set of simulations was made available after many machine-learning models had started to be developed and hence was employed by fewer models.

**Table 1.** The different available training data sets and which machine-learning models used them. Data sets marked with an asterisk were only used for validation and not training by the model. The size of each data set is shown in brackets, other than the EWS random cutouts and the real lenses, since the different models used different numbers of these.

Data set (size)	Model				
	1	2	3	4	5
S1 (11 057 + 10 311)	✓	✓	✓	✓	✓
S2 (5363)	✓	✓	✓	✓	✓
S3 (2143)	✓				
Real lenses	✓	✓	✓*	✓*	✓
DESI spirals (~ 2300)	✓	✓	✓	✓	✓
DESI mergers (~ 250)	✓	✓	✓	✓	✓
DESI rings (~ 60)	✓	✓	✓	✓	✓
DESI LRGs (~ 2700)	✓	✓		✓	✓
DESI others (~ 2300)	✓	✓	✓		
S2 random counterpart (4106)	✓	✓	✓		✓
EWS random cutouts	✓			✓*	

tions of simulations and real lenses, while others were trained on simulations alone and the real lenses were used to validate their performance. For details of how each machine-learning model was trained see Sect. 4.

## 2.2.3. Non-lenses

When curating a data set of non-lenses for machine-learning training, there are two general approaches. Firstly, one can use a collection of random non-lenses, typically with a similar selection function as foreground galaxies used for the simulations, where the idea is that by training on data that resembles the population of objects in real data, it will extrapolate well to the data to which it is being applied. An alternative approach is to recognise objects that are more likely to be mistaken for lenses (such as spiral and ring galaxies) and train the models on these specifically. In Cañameras et al. (2024), it was found that the lens-finding performance of a machine-learning model depends significantly on the contents of the negative set, favouring the use of non-random negative sets.

There were two sets of random cutouts, one of objects in Q1 with the same selection function as the LRGs used for S2 (see Sect. 2.2.1) containing 4106 objects, and one of objects with the same selection function as Q1 but from EWS tiles that lie outside the Q1 area. There was a set of labelled non-lenses, which primarily originated from a visual inspection of objects with Dark Energy Spectroscopic Instrument (DESI) data available (Euclid Collaboration: Rojas et al. 2025). This provided a data set of approximately 2300 spiral galaxies, 250 mergers, 60 ring galaxies, 2700 LRGs, and 2300 others. The DESI LRGs were the LRGs used for S1 and S3. Table 1 shows all the data sets available along with which machine-learning models used which sets.

## 3. Zoobot: pretrained Bayesian CNN

### 3.1. Model description

Zoobot<sup>2</sup> (Walmsley et al. 2023) is a Bayesian CNN that is pretrained on 92 million morphological classifications of galaxies as part of the Galaxy Zoo citizen science project (Lintott et al. 2008). Using pretrained models such as Zoobot and fine-tuning them is an example of ‘transfer learning’, where by taking a tool

<sup>2</sup> <https://github.com/mwalmsley/zoobot>

that is already primed to solve a different but related problem and then adapting only a part of the model, it is possible to create a model that is optimised to solve a new problem in a way that is quicker and easier than creating a model from scratch (Walmsley et al. 2024). In our case, we take the pretrained base Zoobot CNN model with pre-determined weights and fine-tune it by freezing all the parameters except those in the final layers. These parameters in the final layers are allowed to vary through training the CNN on new data such as images of strong lenses. The idea of using Zoobot as a base model for lens finding was first presented and tested by Pearce-Casey et al. (2024), where it was found to be the best-performing machine-learning model of the 20 models tested on *Euclid* ERO data; this motivated the use of Zoobot for lens finding in Q1.

The base Zoobot model was not built to detect lenses originally, nor was it developed on *Euclid* data. However, lens finding in *Euclid* is still a morphological classification task using astronomical images. Many of the features of the latent space that Zoobot uses to distinguish the features of galaxy morphology are likely to be relevant to lens finding. While Zoobot will have seen very few images of lenses, it has been pretrained on huge numbers of non-lenses that are likely to be common in the *Euclid* data set, making it primed to detect these. Pretrained models are especially powerful in tasks such as strong lens finding where the lack of known lenses to train on is a significant issue; fine-tuning a model requires significantly less training data to learn from than a usual model would, and while the number of simulated lenses available is much greater than the number of real lenses, it is still limited. Using a pretrained model also greatly reduces the chance of overfitting as the model is already primed to pick out useful morphological features; Zoobot should already be able to infer what parts of an image are relevant for classification and what to ignore as background objects, artefacts, or stars. By keeping the first layers from the pretrained Zoobot, this also ensures that the model is encouraged to learn true morphological properties rather than other patterns that may arise in simulated lenses such as PSF orientation (Wilde et al. 2022).

There are many different pretrained architectures of Zoobot available. The version employed in this work is the ConvNeXT-Nano version, since it performs well while being quick to train, with 15.6 million trainable parameters. The ConvNeXT architecture is based on the foundational ResNet-50 model, but ‘modernised’, incorporating elements from vision transformers to improve performance while retaining the strengths of CNNs such as simplicity (see Liu et al. 2022 for more details). There were both greyscale (one channel input) and colour (three channel input) pretrained versions of this model available and we used the respective version to match the type of images with which we fine-tune Zoobot.

### 3.2. Fine-tuning approach

There were many different variables that could be adjusted to improve the performance of Zoobot when fine-tuning it from a general morphology classifier to a strong lens finder. These included the choice of training data, the choice of what types of images (scalings and filters) to use, and machine-learning hyperparameters (such as batch size and the number of layers fine-tuned). The framework that we used to build an optimal version of Zoobot involved selecting one choice for each of the mentioned options, fine-tuning this version of the model on the choice of training data, and then evaluating each version by its performance on real lenses and non-lenses. This consisted of 97 known grade A *Euclid* lenses and a data set of 26 222 non-lens *Euclid* cutouts

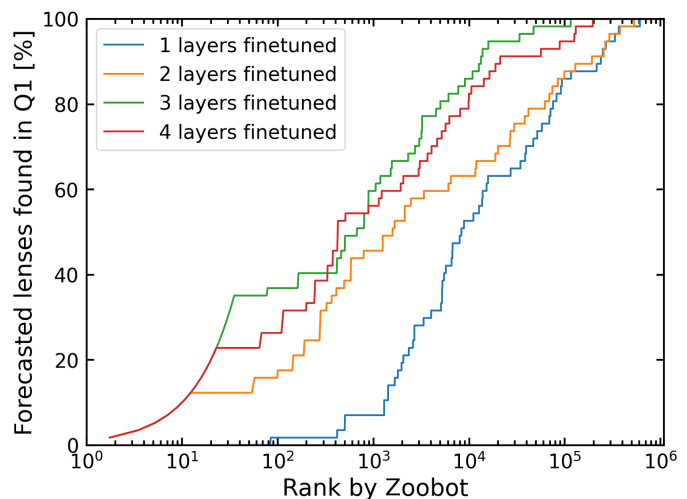


**Fig. 2.** The forecasted performance of different versions of Zoobot when changing the number of layers that were fine-tuned. Numbers are based on the performance on the sample of known lenses in *Euclid* and cutouts from random EWS tiles outside Q1, with the statistics extrapolated to predict the performance in Q1.

from EWS tiles outside Q1 (see Sect. 2.2.3). Since the ratio of 97:26 222 does not reflect the proportion of lenses expected in real *Euclid* data, we scale the statistics to match the ratio of expected lenses according to Collett (2015). For each fine-tuned version of Zoobot, we rank order all of the 26 222 + 97 cutouts. To compare the different versions, we plot (e.g., see Fig. 2) as a function of Zoobot rank the cumulative fraction of the 97 lenses recovered against the total number of images up to that Zoobot rank. This allows us to forecast the number of lenses we should find in Q1 as a function of how many objects we have to inspect.

The different versions of the models were compared according to the fraction of lenses recovered after inspecting 0.01%–0.1% of the data. This corresponds to 1000–10 000 images over the entirety of Q1, roughly our expected expert and citizen scientist inspection capacity. Typically, machine-learning models have their performance evaluated by zero-dimensional quantifiers, such as the area under receiver operating characteristic (ROC) curve. However, because we have a limited visual inspection budget we are only interested in the performance in a specific range; if we are only able to visually inspect  $n$  images, it makes no difference if the lenses that were missed were ranked at  $n + 1$  or  $n + 1\,000\,000$ . Therefore, using metrics that value the performance across the whole range of ranks equally is less useful than inspecting the performance in a range of ranks that corresponds to what can be visually inspected.

#### 3.2.1. Hyperparameter tuning

One hyperparameter that was specific to the pretrained model which was found to make a significant impact on performance was the number of layers that were fine-tuned. The more layers that are fine-tuned, the less the model relies on what was learnt during pretraining, but the more it can adapt to the new data. In order to find the optimal number of layers to fine-tune, we allowed this to vary while keeping the other hyperparameters constant, and the performance of the different versions are plotted in Fig. 2. We found that the number of lenses recovered at a certain rank increases as the number of fine-tuned layers increases up to three, but increasing the number of fine-tuned layers from three

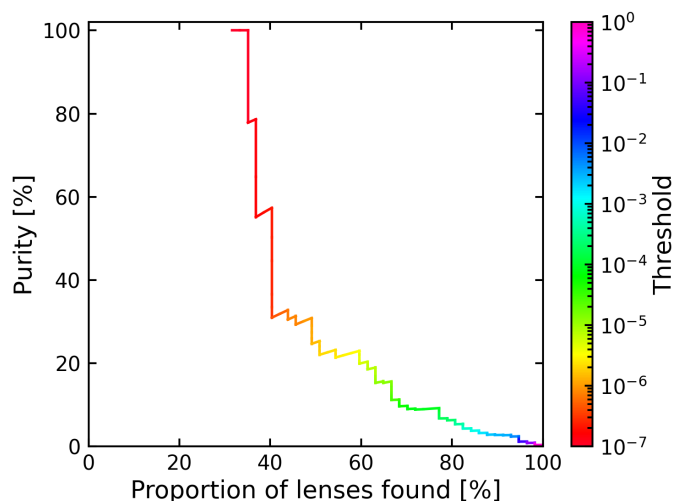


**Fig. 3.** Purity and proportion of lenses found (or TPR) for lenses scored by Zoobot at different thresholds, as evaluated on the validation data set of known lenses after being rescaled to the forecasted lens rate.

to four resulted in a decrease in the number of lenses recovered in the range of ranks we are interested in (specifically  $10^3$ – $10^4$ ). As such, we chose the version with the last three layers fine-tuned as the best model. This fine-tuning performance makes sense; fine-tuning too few layers requires the classifier to closely resemble the original Zoobot classifier, which is not designed for lens finding, whereas fine-tuning too many layers erases more of the useful features of astrophysical data that Zoobot has learnt from millions of Galaxy Zoo classifications.

Other choices such as batch size, learning rate, and choice of image scalings were also found to affect performance. Similarly to the number of layers fine-tuned, we varied these hyperparameters and compared the performance of the different versions of the model to determine the optimal choice for each. In terms of image scalings, it was found that for  $I_E$ -only greyscale images, the arcsinh scaling resulted in a better performance than the MTF scaling, and the  $I_E$ -only greyscale images generally performed better than the multi-band colour images. It was found that the optimal values of batch size and learning rate were 64 and  $10^{-4}$  respectively, and these were used for the final version of the model for the Q1 lens search. However, it is likely that the optimal hyperparameters found here are specific to this training set and as such are likely to be different to what is optimal in future *Euclid* lens searches when we will be able to train new versions of the machine learning models using the lenses found in Q1.

### 3.2.2. Training data set selection

While the possibilities of combinations of data sets to use in training was large, we found that the best performance came when training Zoobot on a combination of S1 and S2 as the positives, and the best set of negatives was the labelled DESI non-lenses. We also implemented the default Zoobot augmentation of images, which includes random rotations, vertical flips, and off-centre cropping and resizing.

We notably found that adding more sets of simulations to the training data did not always improve performance, demonstrating that for pretrained models, the performance is not necessarily constrained by the quantity of training data as much as the quality of it. However, for other models that are not pretrained and

therefore typically require larger training sets, this may not be the case.

Additionally, we found that using a smaller but more selective data set of negatives, where each object had been labelled and the proportion of commonly misclassified false positives (such as ring galaxies and spiral galaxies) had been inflated, resulted in a performance that appeared to generalise better than a model trained on random cutouts. It was also found that training on these labelled non-lenses alone resulted in better performance than a combination of labelled non-lenses and random cutouts, again suggesting that a quality-over-quantity approach is preferable for pretrained models.

### 3.3. Results from fine-tuning

To quantify the performance of a model, statistics that are of particular interest are the true positive rate (TPR), false positive rate (FPR) and purity ( $P$ ),<sup>3</sup> given in terms of true positives ( $N_{TP}$ , number of lenses that were predicted to be lenses), false positives ( $N_{FP}$ , number of non-lenses that were predicted to be lenses), true negatives ( $N_{TN}$ , number of non-lenses that were predicted to be non-lenses), and false negatives ( $N_{FN}$ , number of lenses that were predicted to be non-lenses):

$$\text{TPR} = \frac{N_{TP}}{N_{TP} + N_{FN}} ; \quad (1)$$

$$\text{FPR} = \frac{N_{FP}}{N_{FP} + N_{TN}} ; \quad (2)$$

$$P = \frac{N_{TP}}{N_{TP} + N_{FP}} . \quad (3)$$

TPR can be thought of as the fraction of real lenses that the machine-learning model predicted to be lenses, FPR as the fraction of non-lenses that the machine-learning model predicted to be lenses, and purity as the fraction of things that the machine-learning model predicted to be lenses that are real lenses. Since machine-learning models do not generally produce a binary (lens/non-lens) output, but rather give objects a continuous score from 0 to 1 of how likely an object is to be a lens, the purity, TPR, and FPR vary according to a score threshold at which to split the objects into lenses and non-lenses. There is generally a trade-off between purity and TPR; by setting a high score threshold, fewer objects are classified as lenses and so the proportion of total lenses found is lower, but as the score threshold is lower the purity decreases. The purity at different TPR values for the best performing version of Zoobot is displayed in Fig. 3. As before, these statistics are calculated based on the performance on the known lenses and a set of random Q1 cutouts, with the purity scaled to take into consideration the expected ratio of lenses to non-lenses in such a sample. We recover an almost entirely pure sample of 35% of the lenses, but the purity falls to 20% to recover up to 60% of the known lenses. As can be seen in Fig. 2, the best version of Zoobot requires the first 10% of all the data (score threshold in the range 0.2–1.0) to be inspected to reach a TPR of 100%.

When Zoobot was applied to the *Euclid* ERO data in Pearce-Casey et al. (2024), Zoobot was found to perform better than the

<sup>3</sup> TPR is also known as recall or sensitivity; purity is also known as precision.

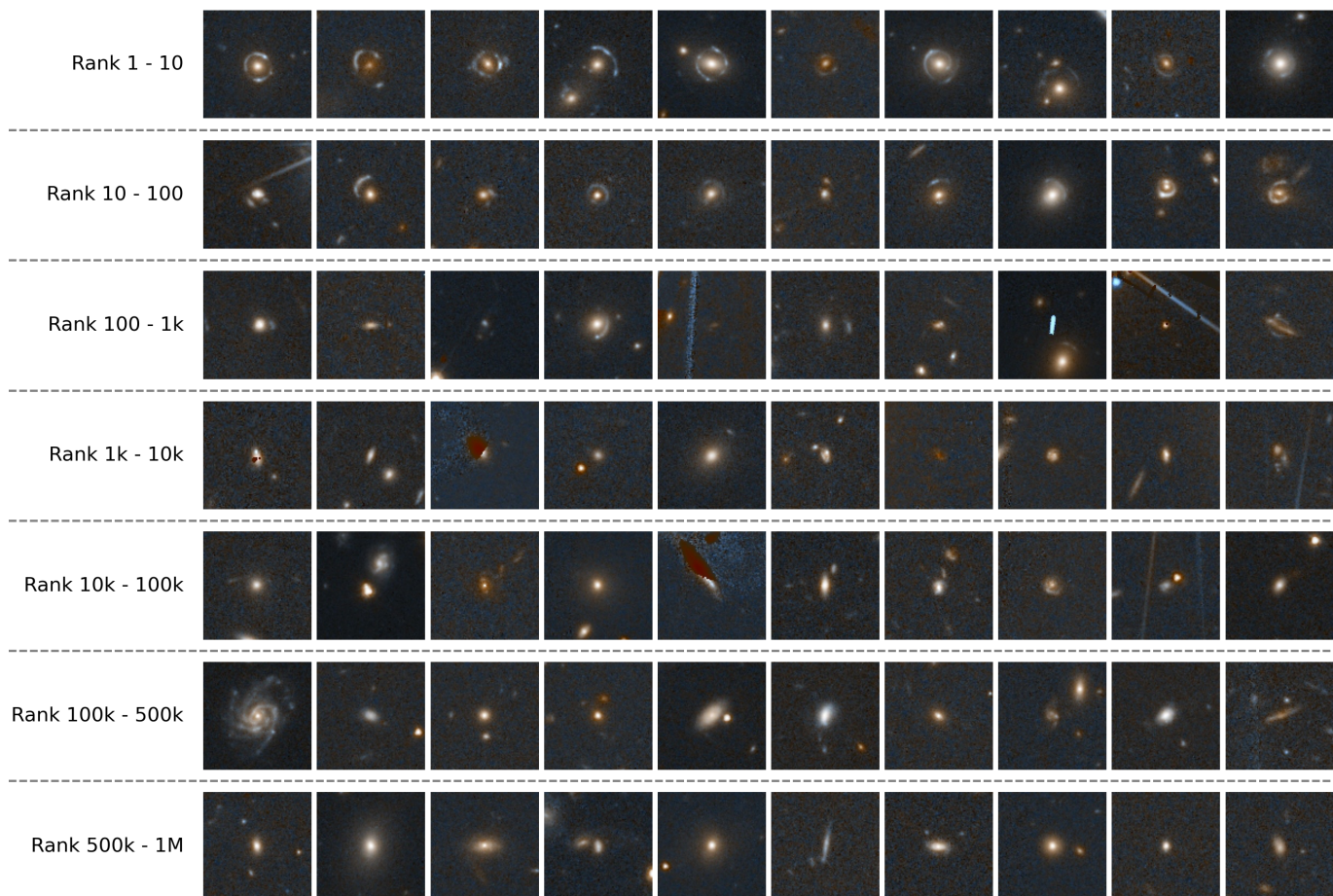


**Fig. 4.** Random images ranked by Zoobot at different ranges of ranks.

other models tested. However, they found that the purity of the lenses discovered was low, which may be partly due to the fact that the number of fine-tuning layers was set to one and was not allowed to vary. Additionally, since the *Euclid* ERO lens-finding experiment there has been significant development in simulations of *Euclid* lenses (e.g., [Euclid Collaboration: Rojas et al. 2025](#)), which is likely to also contribute to a discrepancy in performance between *Euclid* ERO and Q1 lens searches. Other factors, such as the limited amount of available *Euclid* data at the time, training only on random cutouts as negatives instead of a curated set of non-lenses, as well as subsequent improvements to the Zoobot base models ([Walmsley et al. 2024](#)), may also contribute to this.

Figure 4 displays random Q1 images at different samples of rankings according to Zoobot. The model is unable to perfectly split the sample into lenses and non-lenses, with non-lenses still contaminating the highly ranked images, meaning that visual inspection is still an essential part of finding strong lenses. However, it is reassuring that at the higher ranks, not only is the density of lenses higher, but it also appears that the lenses that are found are typically more obvious lenses, whether that is due to a high signal-to-noise ratio or a large Einstein radii creating a clear distinction between the lens and arc light. We do not find that the false positives are dominated by spirals, which has historically been a problem for lens finding, and this is likely due to the fact that Zoobot had been pretrained to recognise a diversity of spiral morphologies. Rather, we find that other than a few artefacts, most of the false positives are chance alignment of

galaxies; examples of highly ranked false positives by Zoobot are shown in Appendix C.

## 4. Other models

In addition to Zoobot, four other models were developed to find lenses in *Euclid* Q1. In this section we provide a brief overview of each model and refer the reader to the original papers in which they were developed. The models are numbered as follows: Model 1 is a 4-layer CNN; Model 2 is OU-100; Model 3 is IncNet; Model 4 is Zoobot (previously described); and Model 5 is LensVision. This does not provide an exhaustive list of all the machine-learning models that are employed to find lenses in *Euclid* in general; additional networks were used in the lens search within the ERO data ([Pearce-Casey et al. 2024](#)), but were not applied to the Q1 data due to time limitations.

### 4.1. Model 1: 4-Layer CNN

Model 1 is a shallow 4-layer CNN, with the architecture used being an adaptation of the network developed for the morphological classification of galaxies in [Domínguez Sánchez et al. \(2018\)](#). It has already been tested with *Euclid*-like simulations ([Manjón-García 2021](#)) and with the ERO fields ([Pearce-Casey et al. 2024](#); [Nagam et al. 2025](#)). The network has four convolutional layers of different spacings ( $6 \times 6$ ,  $5 \times 5$ ,  $2 \times 2$ , and  $3 \times 3$ , respectively), and two fully-connected layers. ReLU activation functions are applied after every convolutional layer, and a  $2 \times 2$

max-pooling is applied after the second and third convolutional layers.

The model was trained on a combination of S1, S2, and S3, and also 80 known grade A and B *Euclid* lenses as the set of positives. For the negatives, a combination was used of random Q1 galaxies matching the selection function of S2, all the LRGs selected for S1, the labelled DESI non-lenses, and also 7378 cutouts of random *Euclid* galaxies from non-Q1 tiles. Two versions of the model were trained, both using  $100 \times 100$   $I_E$ -only images with fluxes normalised from 0 to 1, but one used the MTF scaling and the other used the arcsinh scaling, with the final scores being the average of these two outputs.

The training of the network was carried out following a supervised learning approach. Decisions regarding pre-processing, architecture, and learning parameters were influenced by what was found to work when the same model was applied to the ERO data in [Pearce-Casey et al. \(2024\)](#). In the learning process, a binary cross-entropy loss function was used and was optimised by the Adam stochastic optimisation method ([Kingma & Ba 2015](#)), with a learning rate of  $10^{-3}$ . The models were trained for 40 epochs, using a batch size of 32. In order to prevent over-fitting, several data augmentation techniques were performed during training, allowing the images to be zoomed in and out (0.75 to 1.3 times the original size), rotated, and flipped and shifted both vertically and horizontally. The output of the final convolution layer was flattened and was inputted to a fully-connected layer with dropout probability  $p = 0.5$ . The final fully-connected layer used a sigmoid activation to turn the output scores into lens probabilities.

#### 4.2. Model 2: OU-100

The OU-100 model is another CNN-based model. The network is a modification of OU-200 ([Wilde et al. 2022](#)), removing the final two convolutional layers due to the change in input size between the two models ( $200 \times 200$  versus  $100 \times 100$  pixels). The architecture consists of four convolutional layers of sizes  $5 \times 5$ ,  $5 \times 5$ ,  $2 \times 2$ , and  $2 \times 2$ , each followed by a  $2 \times 2$  max pooling layer, a dropout layer with dropout probability  $p = 0.2$  and a ReLU activation function. This is followed by a fully-connected layer with 350 neurons, followed by an output layer with a soft-max activation function to produce a lens prediction.

The positive training set included S1, S2 and all the 200 known grade A and B lenses. The negative training set consisted of the labelled DESI non-lenses, the remaining LRGs used for S1, and the random galaxies counterpart from S2. A random selection of 40 000 images were selected from the resulting 171 478 images, using the four image options:  $I_E$ -only arcsinh;  $I_E$ -only MTF;  $I_E + Y_E$  MTF; and  $I_E + J_E$  MTF. Of each set of 40 000 images used for training the different versions, 32 000 images were used for training, 2000 used for validation, and 6000 for testing. The network was trained with a batch size of 100 and a learning rate of  $3 \times 10^{-4}$ . A categorical loss is used to classify the images into lens and non-lens classes. Since the training data contains 12% lenses, a weight was applied to give each class an equal weighting during training.

When inspecting the top 100 ranked candidates from the  $I_E$ -only MTF and  $I_E$ -only arcsinh images, it was found that the MTF version appeared better at finding lenses, while lots of the high-ranked objects by the  $I_E$ -only arcsinh version of the model contained stars. In the end the MTF  $I_E$ -only version of OU-100 were used.

#### 4.3. Model 3: IncNet

The IncNet architecture is based on the ‘inception module’ ([Szegedy et al. 2015](#)) that applies convolutions of different size on the images in parallel, to extract features on different scales simultaneously and then combines them. The images are passed through two convolutional layers, alternated with max-pooling layers. After this, they go through seven inception modules. The fifth of them is connected to a classifier whose score is combined with the score of the final classifier (i.e., that at the end of the seven inception modules) to guide the weights update (refer to [Szegedy et al. 2014](#) for a more detailed discussion). The output of the classifiers are weighted differently: 0.3 for the intermediate one; and 1.0 for the final one. This baseline architecture, presented in [Euclid Collaboration: Leuzzi et al. \(2024\)](#), was further modified for the Q1 lens finding challenge to account for the input image sizes of  $100 \times 100$  pixels compared to the original  $200 \times 200$  image sizes it was optimised for, requiring a reduction in the number of filters per layer, while keeping the same number of layers.

For network training, a combination of S1 and S2 was used for the positive class. In the case of S2, the images were augmented by applying either a random rotation or flip to every image. For the negative class, a combination of random galaxies matching S2 and labelled DESI non-lenses were used, with the total number of training images being approximately 40 000. For validating the network, a combination of known grade A and B lenses were used, in addition to a non-overlapping set of negatives from the training data. The images used were the  $I_E$ -only images with the arcsinh scaling. During training, an ADAM optimiser was used with an initial learning rate of  $10^{-4}$  and binary cross-entropy as the loss function. The model was trained for 100 epochs, and although early-stopping was enabled in the training loop to prevent overfitting, it was not needed.

#### 4.4. Model 4: Zoobot

Model 4 is Zoobot, which has been previously described. Refer to Sect. 3 for more details.

#### 4.5. Model 5: LensVision

The final model is the only non-convolutional network developed, instead opting for a vision transformer-based architecture, and similarly to Zoobot employs pretraining. It uses multi-step supervised contrastive learning and a classification head. Input images are divided into  $16 \times 16$  patches, which are flattened and projected into 768-dimensional embeddings. These embeddings are passed through a transformer encoder that processes the relationships between the patches. The transformer encoder is pretrained using a two-step supervised contrastive learning technique. This pretraining helps the model to learn to separate lensing features from non-lensing features by pulling embeddings of similar images closer together and pushing embeddings of dissimilar images apart in the feature space to create a similarity matrix. After the encoder, a fully connected classification head takes the learned image representations and predicts whether the image contains a gravitational lens or not, represented by a score between 0 and 1. The classification head includes dense layers with activation functions and dropout to prevent overfitting. During training, the transformer layers are gradually unfrozen, allowing the model to fine-tune the earlier layers without losing the features learned during pretraining.

**Table 2.** Number of lenses of each grade and non-lenses found in each model’s top 1000 ranked objects, along with the total number of lenses of each grade found in Q1 in total (out of approximately one million).

	Model					Total found in Q1
	1	2	3	4	5	
Grade A lenses	69	24	8	122	3	250
Grade B lenses	34	12	5	41	4	247
Grade C lenses	46	22	1	67	10	585
Non-lenses	851	942	986	770	983	$\sim 10^6$

The data used for training includes S1 and S2, as well as a set of known grade A and B lenses for positives, and the random galaxies matching S2 and the labelled DESI non-lenses as the negatives. This data set was augmented to increase the size by including rotations and corner cutouts of each image. The images used the arcsinh scaling on the  $I_E$ -only images.

## 5. Results

Originally there were approximately  $10^6$  Q1 cutouts which may have contained lenses, and only  $10^4$ – $10^5$  of these could be visually inspected based on the typical engagement in citizen-science projects. Therefore we carried out visual grading of lenses in two rounds. A first preliminary inspection allowed us to evaluate each model’s performance in order to prioritise high-performing models in the selection of images for the second, larger visual inspection round.

First, a group of strong lensing experts within the Euclid Collaboration visually inspected the top 1000 ranked objects from each of the models 1–5, in what is referred to as the Galaxy Judges (GJ) project (Euclid Collaboration: Walmsley et al. 2025). This was to gain an initial understanding of how the models compared in lens finding, and was to inform which models should be prioritised in selecting which candidates were shown to citizens. Following this was the citizen science visual inspection, for which we created a *Euclid*-specific version of the Space Warps (SW) project ran on the Zooniverse platform (Marshall et al. 2015; More et al. 2016). All objects that were ranked highly by these citizens were then added to the GJ project and were ranked by experts, giving the final grades for all the interesting lens-like objects discovered. In both the SW citizen science project and the GJ expert classifications, each image was inspected by multiple humans, with the results being aggregated in order to reduce noise and the level of subjectivity. For SW, the citizens were given the option of lens or not a lens, while in GJ the experts assigned a grade to quantify the quality of a lens. These grades were: X (not a lens); C (contains lens-like features but not obviously a lens); B (probably a lens); and A (confidently a lens). Examples of lenses with these grades are shown in Appendix B. In this paper we focus on using the results from the visual inspection to quantify model performance; for a detailed analysis of the visual inspection process see Euclid Collaboration: Walmsley et al. (2025).

Machine-learning models typically output scores which range from 0 to 1, with 1 corresponding to a high likelihood of being a lens (though not strictly a probability). Similarly to grades, the absolute value of scores across different machine-learning models is arbitrary, so we rank the objects by the scores of each model and compare the ranks.

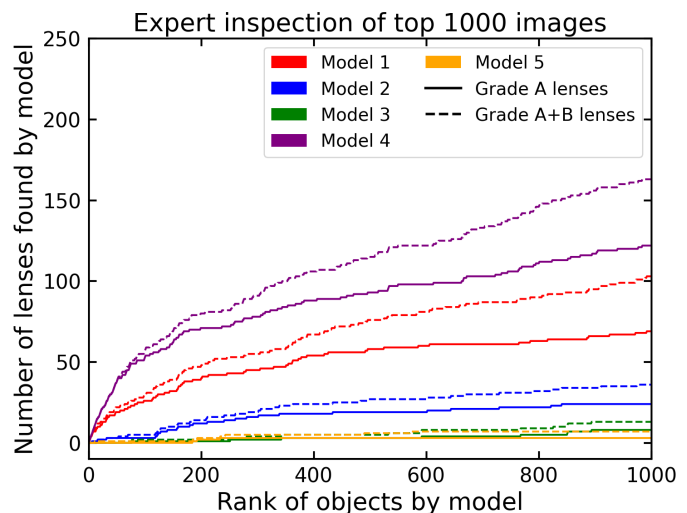


**Fig. 5.** Number of lenses found in the top-ranked objects according to models 1–5. This is shown for grade A lenses (confident strong lenses) and the combination of grade A and grade B lenses (likely strong lenses).

### 5.1. Preliminary expert classifications for model comparison

Each of the five models’ top 1000 objects were ranked by experts, with each cutout receiving approximately 10 votes which were then aggregated into one grade. Note that a rank of 1000 corresponds to different threshold scores for each machine-learning model: the corresponding scores for Models 1–5 are 0.992, 0.999, 0.983, 0.999, and 0.967, respectively. The aim of this was to evaluate each model’s ability to find lenses. The two main areas of consideration in this analysis were: (1) how many lenses of each grade were found by each model; and (2) of the lenses that one model did not rank in its top 1000 object but were highly ranked by another model, where did these missed lenses sit in its score distribution. The first of these is addressed in Fig. 5, displaying the number of grade A and the number of grade A + B lenses found by each of the Models 1–5. The breakdown of the number of lenses and non-lenses in each model’s top 1000 ranked objects is shown in Table 2. The best performing model is Model 4 (Zoobot), discovering almost twice the number of grade A lenses as the second-best performing model, model 1 (4-Layer CNN). Although the other models discover fewer lenses, the proportion of lenses picked out by every model in the top 1000 is significantly higher than the random lens to non-lens ratio (around  $1:10^3$ ). However, the top 1000 ranked images from every model are still non-lenses by majority, meaning visual inspection by humans is essential.

### 5.2. Citizen scientist classifications

Once we had verified that all the models were able to find lenses, we picked the images that were ranked highly by any of the models and uploaded these to a public citizen science SW project on the Zooniverse platform. Here, citizens classified each cutout based on whether they thought it contained a lens or not. This took place over the span of about six weeks, with 857 278 total classifications being made by approximately 1 800 users. Images that were flagged as possible lenses by the citizens were then passed to expert inspection in the GJ project to get a final grade. It was decided to use SW to visually inspect the top 10 000 objects from each model, and once this was completed the next

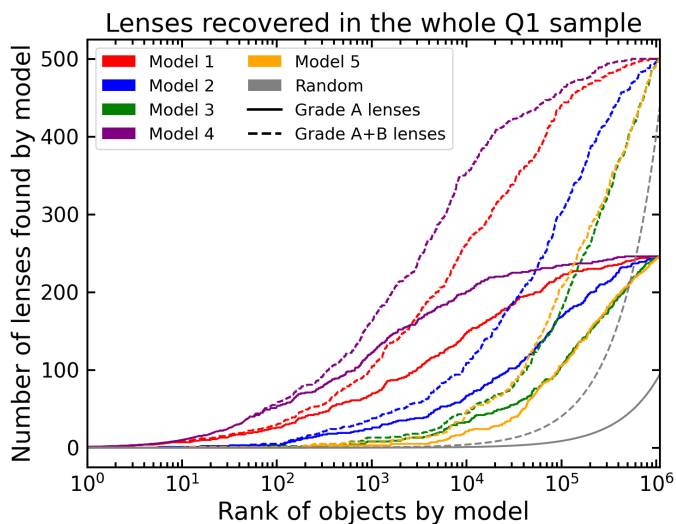


**Fig. 6.** Number of grade A and grade A + B lenses discovered by each model as a function of rank. This is similar to Fig. 5, except extended to the entirety of the million Q1 objects and plotted with a log rank scale. A random distribution of lenses is shown for comparison. Note that unlike Fig. 5, not all the objects at every rank have been graded as lens/non-lens, so this only reports the distribution of lenses given that they have been recognised as a lens.

10 000 from Model 1 and Model 4 were added, along with a subset of the next 10 000 images from the other models.<sup>4</sup> A random sample of 40 000 images was also added for calibration.

Of the 1 086 554 cutouts that we started with, a total of 115 329 objects were inspected by SW, of which a subset of 7362 were graded highly enough to make it to the follow-up expert classification stage. Of these, there were 250 grade A, 247 grade B, 585 grade C lenses, and 6280 non-lenses. The top grade A lenses are displayed in Sect. A.1. Of these, only four grade B and five grade C Q1 lenses appeared in the ‘known real lenses’ data set that some models used for training. Almost all the lenses discovered were from images that were uploaded to SW due to being highly ranked by at least one of the machine-learning models: 2/250 grade A lenses and 8/247 grade B lenses were found in the random images that were not selected for SW by any of the machine-learning models. A distribution of how all these lenses were ranked by each model is shown in Fig. 6. The catalogue of all the lenses we found is publicly available on Zenodo<sup>5</sup>.

### 5.3. Completeness of our lens sample

In addition to uploading highly ranked images that had been selected by the machine-learning models, we also uploaded 40 000 randomly-selected images from the original 1 086 554 Q1 images. This allowed us to quantify how good the machine-learning models are at finding lenses and forecast how many lenses we would have found had we visually inspected the full Q1 sample. Note that this random sample necessarily had a small overlap with the machine-learning-selected sample, since otherwise it would have contained less lenses than average. Within this random sample we found 9 grade A lenses and 22 grade B lenses, although many of these random images had also been selected by the machine-learning models.

<sup>4</sup> The specifics of SW are outlined in the system overview paper (Euclid Collaboration: Walmsley et al. 2025).

<sup>5</sup> <https://doi.org/10.5281/zenodo.15003116>

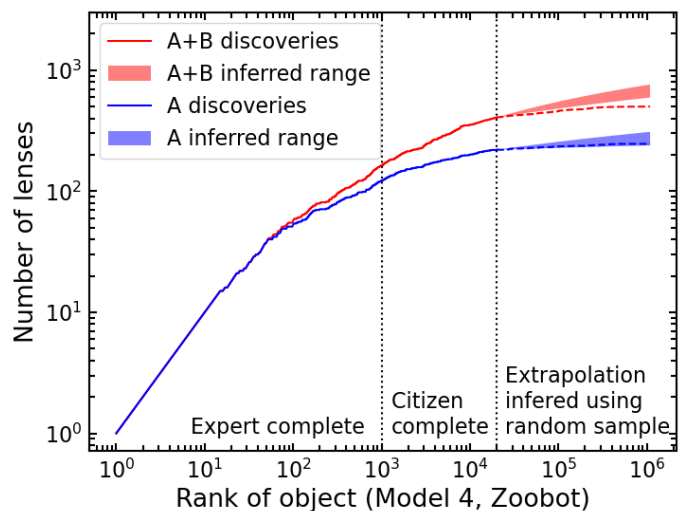


**Fig. 7.** Performance of Zoobot, accounting for uninspected images. The first 20 000 objects have been inspected by citizen scientists. Beyond 20 000 the performance is extrapolated based on the prevalence of grade A and B lenses on a randomly selected, citizen-inspected sample of images. The dashed lines show lenses discovered by the inspection of multiple networks detailed in Euclid Collaboration: Walmsley et al. (2025). The gap between the dashed line and the band shows the likely rank of undiscovered lenses in Q1.

We can use Bayes’ theorem to infer the rate of lenses in the total sample, given that we found 9 grade A and 22 grade B lenses in a sample of 40 000. Assuming a log-uniform prior on the rate of lenses between 0 and 1 we infer  $240^{+90}_{-70}$  grade A lenses and  $540^{+130}_{-120}$  grade B lenses (68% confidence). The overall system found 250 grade A lenses and 247 grade B lenses (497 grade A + B), indicating that some grade B lenses may have been missed, but that it is likely that we discovered almost all grade A lenses. A substantially better estimate of the total number of lenses in Q1 can be made by including the fact that we have complete knowledge of how the system performs up to a Zoobot rank of 20 000. This is the regime where most lenses exist, but it is sparsely probed by the random sample. Given that the random sample included 2 grade A lenses beyond this point, we can infer that Zoobot missed  $45^{+43}_{-26}$  grade A lenses (68% confidence). For grade B, Zoobot’s top 20 000 misses  $289^{+97}_{-79}$  lenses. The combination of the other four machine-learning models found 26 of the grade A lenses and 68 of the grade B lenses that Zoobot missed.

The binomial estimates in the previous paragraph allow us to estimate where the Zoobot ROC curve should end. We do not know how the ROC curve should evolve between 20 000 and the final image, but it is likely that the rate of missing grade A and B lenses decreases with Zoobot rank. Figure 7 shows the range of ROC-like curves for Zoobot that are consistent with the binomial estimates and assuming the probability of finding a lens is proportional to the Zoobot rank between 20 000 and the final image.

Furthermore, it is important to understand the completeness of this sample as a function of properties such as brightness and Einstein radius. An analysis of this for the full Q1 lens catalogue is presented in Euclid Collaboration: Walmsley et al. (2025), but we will be able to do this for specific machine learning models in the future when we have enough real lenses to sufficiently span this parameter space.

## 6. Discussion

### 6.1. Machine-learning takeaways

Of the models trained, all of them used both S1, S2, and the labelled DESI non-lenses. The remaining data sets used by some but not all models included the real known lenses and other random cutouts. While it was found during the training of Zoobot that adding additional simulations and sets of random cutouts to the training often decreased the performance, the second-best performing model (Model 1) notably used all the available data sets for training. While Model 1 and Zoobot both are CNN-based models, Zoobot implemented pretraining which likely changes how the training data affects performance, and as such it is hard to draw any conclusions about what training data are best for lens finding in general.

A similar case is that of image scalings, which again varied across models and did not appear to directly correlate with machine-learning performance. Zoobot found that when using  $I_E$ -only images, the arcsinh scaling resulted in a better performance than MTF, while Model 2 found that the arcsinh scaling picked out more stars and performed worse than the MTF scaling. Models 3 and 5 used the arcsinh  $I_E$ -only images, and Model 1 trained  $I_E$ -only models for both the arcsinh and MTF scaling and averaged the results. Although colour images were available, all teams decided to use the  $I_E$ -only greyscale images in the best versions of their models, despite many teams also testing colour-based models. This is of interest as during human visual inspection, it is often found that colour aids in the detection of lenses, since there is typically a red/blue gradient between the lens/source galaxy that is helpful for distinguishing lenses. The fact that no team found there to be a significant improvement in performance when adding colour data may suggest that machine-learning models prioritise different aspects of images when classifying lenses, or alternatively that these models are not able to pick up on properties such as colour gradients as well as they are able to pick up on morphological information. The latter may make sense in the case of Zoobot; through being pretrained on galaxies of different morphologies, it is not clear that there would be any pattern in colour information that could be extrapolated to lenses in the way that patterns picked up in morphology may be useful. Patterns picked up in the difference between intensities in different filter bands likely might be something that happens in the first few layers of a network and therefore is not something that fine-tuning can address.

Figure 8 shows the position of grade A lenses as a function of Model 1 and Model 4 rank. The two ranks are broadly correlated, but with substantial scatter. It is not clear if the scatter is due to the networks learning different features, or due to the intrinsic uncertainty of each model. We colour each of the points according to the model that best ranked each grade A lens. This can be seen as a marker for which network would have discovered it first. Models 1 and 4 combined make up the large majority of the grade A lens first discoveries (88%) and the combination of them results in a powerful lens finder. Many grade A lenses beyond Model 1's top 20 000 were highly ranked by Model 4 and vice versa. While Models 2, 3 and 5 were able to provide additional lenses, only 7 were beyond the 20 000 inspection threshold of Models 1 and 4. These results suggest that Models 1 and 4 provide the bulk of the discovery information. Future searches should use a verification set to check machine-learning performance and use that performance to prioritise the visual inspection effort between networks, or to build an ensemble classifier (Euclid Collaboration: Holloway et al. 2025).

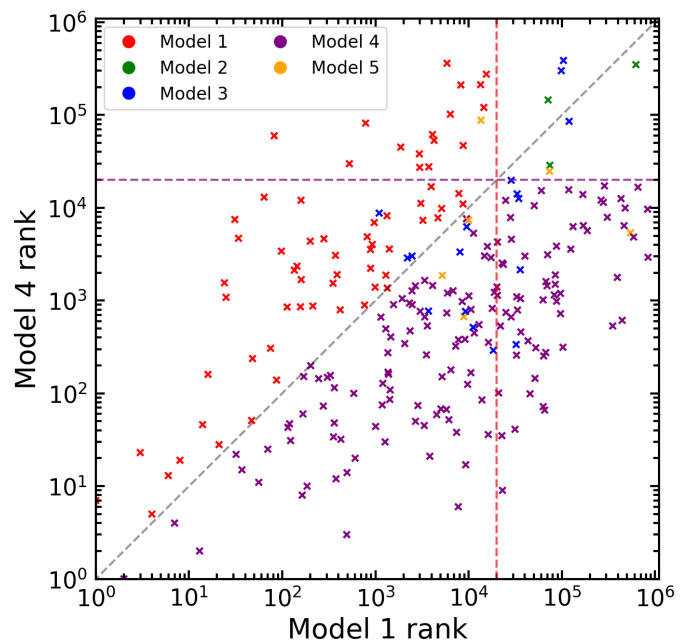


**Fig. 8.** Rank of the grade A lenses by Models 1 and 4. The colours indicate which of the five models ranked each grade A lens the highest. The vertical and horizontal lines at rank 20 000 mark the limit of the visual inspection for Models 1 and 4.

### 6.2. The future of lens finding in Euclid

With the number of lenses discovered thus far, it is evident that a large number of strong lenses in *Euclid* are discoverable, and the future releases of *Euclid* data are going to contain a wealth of interesting data for strong lensing. However, while the number of lenses will scale with the amount of data *Euclid* collects, the number of objects that can be visually inspected by humans will remain roughly constant, providing a challenge for lens finding as long as humans remain better at recognising strong gravitational lenses than machine-learning algorithms.

The number of objects able to be classified by humans in the SW project was around 100 000, meaning 10% of the Q1 data was visually inspected. However, the *Euclid* DR1 data will cover around 2000 deg<sup>2</sup> of the EWS (40 times the area of Q1), and hence visually inspecting 100 000 objects will only make up 0.25% of the total DR1 data. Previous lens-finding citizen-science projects have been able to search through a larger number of images (e.g., 430 000 in the CFHT Legacy Survey SW project; see More et al. 2016), so assuming an upper limit of visually inspecting one million objects, it is therefore informative to investigate what lenses fall inside/outside the top 0.2%–2% of Q1 (corresponding to the top 2000–20 000 objects).

In the left panel of Fig. 9 we present the density of lenses found in Q1 as a function of Zoobot rank. Although there will be lenses in Q1 that we did not discover, as explained in Sect. 5.3 almost all grade A lenses were likely discovered and hence we can take the frequency of the discovered grade A lenses as being the true frequency. The worst rank of a grade A lens according to Zoobot is 466 371, meaning Zoobot alone is unable to discover 100% of the grade A lenses in DR1. However, 152 (220) of the grade A lenses were ranked in the top 2000 (20 000) by Zoobot, meaning the number of grade A lenses in DR1 that we will be able to discover with the help of citizen science is around 7500–11 000, which will be by far the largest collection of strong lens candidates at the time. Looking beyond DR1, in the full *Euclid*

6-year survey the top million ranked Zoobot objects will contain 75 000 grade A/B lenses, providing a revolution for strong lensing.

These DR1 forecasts assume that the models used here are the best we can do at lens finding. However, different machine-learning models have different strengths and weaknesses when it comes to lens finding, so by analysing the abilities of different models it is possible to create an ensemble classifier that is better than the sum of its parts. In [Euclid Collaboration: Holloway et al. \(2025\)](#), it was found that by combining Zoobot with Models 1 and 2, the resulting ensemble classifier outperforms Zoobot alone at lens finding in Q1. Additionally, as the number of known lenses grows, we will be compiling an increasingly large sample of real *Euclid* strong lenses that we can include in our training, which is likely to improve the lens-finding abilities of all the machine-learning models. As such, the numbers forecasted here should provide a lower limit of performance.

### 6.3. Discovery of lenses of particular interest

An ensemble approach to lens finding will still benefit from the individual machine-learning models being optimised as much as possible, and one aspect that is worth considering is the ability to discover lenses of individual scientific value. Figure 9 shows the rank and the corresponding images of objects that may be more interesting than the typical single-galaxy-lensed-by-an-LRG lensing configuration that dominate the strong lens samples and are typically the only type of lens system that is simulated. It is interesting to investigate how these objects are scored by machine-learning models which are not trained to recognise lenses of this type.

#### 6.3.1. DSPLs

DSPLs are useful cosmological probes; an analysis and modelling of the DSPLs found in *Euclid* Q1 is presented by [Euclid Collaboration: Li et al. \(2025\)](#). There it was found that four lenses in Q1 could be convincingly modelled as DSPLs, and there were another four candidate DSPLs. The ranking of the four DSPLs by each of the models is presented in Table 3, and images of these four DSPLs are shown in Sect. A.2. Although four DSPLs is not enough to confidently extrapolate about our ability to discover DSPLs in the EWS, it is reassuring that many of them were ranked highly. Model 1 performs exceedingly well at picking out the DSPLs, with all four of them being ranked in the top 500. With the combined performance of the five models it is unlikely that we missed many high-quality DSPLs, with only  $6 \pm 3$  forecasted to be detectable within Q1 to begin with ([Euclid Collaboration: Li et al. 2025](#)).

Although worse than Model 1, Zoobot also performs well at recovering DSPLs, with two of the four DSPLs being in the top 10 ranked objects (top 0.001%), at ranks 3 and 7. The ranks of the other two DSPLs were 1902 and 2349, which although sitting at the lower end of the grade A lens ranks, still ranked highly enough for all of them to likely be recovered if they were in DR1. Of the four DSPLs, the two that were ranked in the top 10 both have a larger Einstein radii, with brighter arcs that are more easily distinguishable than the two lower ranked. The DSPL candidates on average rank lower, with ranks of 622, 1540, 4277, and 24 853, and also have smaller Einstein radii, fainter arcs and/or lens light blending with the arc light. Although only candidate DSPLs, these are still systems that we are interested in, and the fact that these are all ranked on the lower end amongst the lenses

**Table 3.** How the four DSPLs in Q1 were ranked by each of the models, following the nomenclature presented in [Euclid Collaboration: Li et al. \(2025\)](#).

	Model				
	1	2	3	4	5
Teapot lens	144	15 214	310 534	2349	417 140
Cosmic dartboard	388	36 156	894	1902	56 723
Galileo’s lens	492	302	6452	3	45 497
Cosmic ammonite	1	241	6141	7	78 550

ranked by Zoobot (though still in the top 2.5% of the whole sample), this may be something we want to address in future machine-learning training.

#### 6.3.2. Edge-on lenses

A similar case can be made for the edge-on disc lenses. As LRGs make up the majority of lens galaxies and typically are easier to simulate accurately, machine-learning models are not generally trained on other types of lens galaxies. Edge-on disc lenses are rarer amongst strong lenses, since disc galaxies typically have lower masses and therefore smaller Einstein radii, and they visually appear quite different to the average lens, especially at high inclination. In the right panel of Fig. 9 we show a sample of eight of the more visually obvious edge-on disc lenses. Because there is not a clear distinction between edge-on disc lenses and regular LRG lenses, especially in the case of lenticular galaxies, it is hard to report the exact number of these in our Q1 lens sample. However, we estimate it to be around 20–30, given an inspection by two experts of the top 1000 GJ-graded lenses, which is consistent with the number from SW (during SW, citizens were given the option to provide tags to images of interest, and 29 had been tagged as ‘#edge-on’). In Sect. A.3 we display some of the grade A/B lenses where the lens galaxy is an edge-on disc or lenticular galaxy. Given how different these can appear to the simulated lenses, it is perhaps not surprising that edge-on disc galaxies are ranked low by Zoobot, even compared to the grade C lens frequency, though they are still picked out at a significantly higher rate than random.

Previous lens finding efforts have not focused on edge-on discs, mostly because the number previously known was very small: the Sloan Wide Field Camera Edge-on Latetype Lens Survey (SWELLS) found 16 grade A and 1 grade B strong lensing disc galaxies ([Treu et al. 2011](#)), while a search within UNIONS found four grade A and 36 grade B edge-on disc lenses ([Acevedo Barroso et al. 2024a](#)). However, edge-on disc lenses are particularly good probes of dark matter, being able to examine properties such as the mass density profile slope and axial ratio of the dark matter halo ([Treu et al. 2011](#)), and the number density of edge-on disc lenses alone is able to distinguish between theories of dark matter and modified gravity ([Harvey-Hawes & Galoppo 2024](#)). Since disc galaxies have to be much more massive than average to act as strong gravitational lenses, disc lenses provide a probe of a rare population of galaxies ([Tortora et al. 2019](#)). Other more complex lensing configurations such as Einstein zig-zags (theorised by [Collett & Bacon 2016](#) and first observed by [Dux et al. 2024](#)) are also likely to exist within the data that *Euclid* collects, and it therefore may be required for us to include such rarer lensing configurations in our training sets in the future.

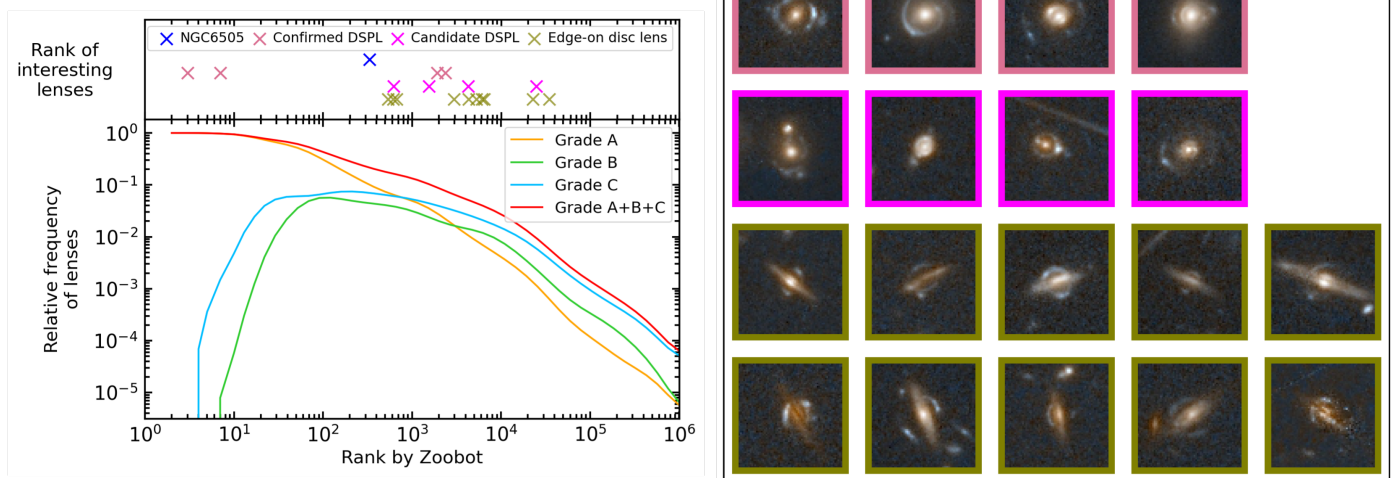


**Fig. 9.** (a) *Left panel, bottom:* density of grade A, B and C lenses found in Q1, as well as the three combined, as a function of Zoobot rank. *Above:* ranks of lenses of particular interest, including the only discovered lens around an NGC galaxy, four confirmed DSPLs, four candidate DSPLs, and 10 of the more visually obvious edge-on disc lenses. (b) *Right panel:* images of the interesting lenses corresponding to objects that are plotted on the left. The images are ordered in increasing rank order left to right (left to right on the penultimate row then left to right on the last row for the edge-on disc lenses).

### 6.3.3. NGC 6505

Although the image configuration is typical, the NGC 6505 lens discovered in O’Riordan, C. M. et al. (2025) is notable as a very low-redshift lens. The lens is thus much brighter than is typical in our training set, with the Einstein ring in the very core. Such low-redshift lenses are valuable because they provide a unique probe of the mass profile of the centre of a galaxy and therefore the stellar initial mass function, and because they provide good constraints on the kinematic properties of the galaxy, they can provide a test of general relativity (Collett et al. 2018). The NGC 6505 lens was discovered in *Euclid* data serendipitously (O’Riordan, C. M. et al. 2025), but it is reassuring that had this not happened it would have still been discovered by the strong lensing discovery engine, being ranked 332 by Zoobot.

## 7. Conclusions

In this work we have presented an analysis of the performance of different machine-learning models at finding strong lenses in the *Euclid* Q1 data covering 63 deg<sup>2</sup>. We compared five different models and investigated some of the factors that can improve the lens finding abilities of the machine-learning models. In combination with expert visual inspection and citizen science efforts, we were able to obtain a large number of lenses and evaluated the performance of the machine-learning models against this. We also explored the abilities of machine-learning models to find different types of lenses and explored how this may scale to the next *Euclid* data releases. However, we have tested the ability of machine-learning models to identify images that an expert human would classify as a grade A or B lens. We have ignored the fallibility of expert humans at lens finding (Rojas et al. 2023). It is possible that some real lenses were identified as such by the machine-learning models yet graded poorly by humans, or that

some non-lenses were identified as lens candidates by the human inspectors.

The machine-learning models presented in this work all perform well at finding lenses, which is significant given the rarity of strong lensing. The best performing machine-learning model is Zoobot, a model pretrained on general (non-lens) galaxy morphologies in non-*Euclid* data. Of the million Q1 objects that were searched through, Zoobot found 122 grade A, 41 grade B and 67 grade C lenses in the top 1000 ranked objects. By fine-tuning the pretrained model, we can transfer the features it has learned about galaxies in general to the specific problem of lens finding, producing a model that required less training data than training a model from scratch (needing only around 10<sup>3</sup> images to train). Using a less data-hungry model meant that we could more deliberately curate the training data set, which was found to be beneficial.

We used the machine-learning models to inform the selection of approximately 100 000 cutouts that were visually inspected by citizens and validated by experts. These images contain the top 20 000 ranked by Zoobot. Within the visually inspected images, we found 250 (247) grade A (B) lenses. Of these lenses, 26 (65) are ranked outside of Zoobot’s top 20 000. However, since we did not visually inspect the full Q1 sample, some inference is required to estimate the number of lenses that were ranked poorly by Zoobot that had not necessarily been found during visual inspection. By analysing a randomly selected subset of the full Q1 sample, we inferred that Zoobot missed 45<sup>+43</sup><sub>-26</sub> grade A lenses (68% confidence) within the full million Q1 sample. For grade B, Zoobot’s top 20 000 misses 289<sup>+97</sup><sub>-79</sub> lenses. The other four networks combined found 26 of the missing grade A lenses and 68 of the missing grade B lenses, meaning we found that the other classifiers add complementary information which explains why an ensemble of classifiers (Euclid Collaboration: Holloway et al. 2025) is more accurate than Zoobot alone.

While machine-learning models are able to pick out atypical lenses such edge-on disc lenses, they are likely to do worse at these than classic configurations of a single source lensed by an elliptical galaxy. We discovered four likely DSPLs, but it is possible that further examples have been missed. Additionally, we find that the best model at discovering DSPLs was different from the model that performed best at finding more regular lensing configurations, further highlighting the benefits of combining multiple machine-learning models. A bespoke search for high value atypical lenses is likely to be beneficial for future lens searches over larger areas.

Collett (2015) forecasted that *Euclid* would have around 170 000 strong lenses discoverable within its footprint. However, at the time it was unknown if there was a tractable method of discovering these; a brute-force method of visually inspecting all 1.5 billion galaxies would take a cumulative inspection time of 48 years at a rate of one image classification per second. Whilst there is plenty of scope for improvement, the fine-tuned version of Zoobot presented in this paper is already sufficiently accurate to find most of the lenses in *Euclid* in a tractable amount of time: by visually inspecting the top million Zoobot ranked objects in the full EWS, we can already expect to find 75 000 grade A/B lenses in just 12 days of cumulative inspection time. The lenses found in Q1 will allow further improvements in the machine-learning models, and by combining different improved machine-learning models we can expect to extract purer samples of lenses from future *Euclid* data releases. These samples will be orders of magnitude larger than what is currently available and will be able to revolutionise cosmological and astrophysical constraints from strong lensing.

**Acknowledgements.** NEPL is supported through a graduate studentship from the UKRI STFC and the University of Portsmouth. This work has received funding from the European Research Council (ERC) under the European Union’s Horizon 2020 research and innovation programme (LensEra: grant agreement No 945536). TEC is funded by the Royal Society through a University Research Fellowship. A.M.G. acknowledges the support of project PID2022-141915NB-C22 funded by MCIU/AEI/10.13039/501100011033 and FEDER/UE. SS has received funding from the European Union’s Horizon 2022 research and innovation programme under the Marie Skłodowska-Curie grant agreement No 101105167 — FASTIDIoUS. Numerical computations were carried out on the SCIAMA High Performance Compute (HPC) cluster which is supported by the ICG and the University of Portsmouth. The Euclid Consortium acknowledges the European Space Agency and a number of agencies and institutes that have supported the development of *Euclid*, in particular the Agenzia Spaziale Italiana, the Austrian Forschungsförderungsgesellschaft funded through BMK, the Belgian Science Policy, the Canadian Euclid Consortium, the Deutsches Zentrum für Luft- und Raumfahrt, the DTU Space and the Niels Bohr Institute in Denmark, the French Centre National d’Etudes Spatiales, the Fundação para a Ciência e a Tecnologia, the Hungarian Academy of Sciences, the Ministerio de Ciencia, Innovación y Universidades, the National Aeronautics and Space Administration, the National Astronomical Observatory of Japan, the Nederlandse Onderzoekschool Voor Astronomie, the Norwegian Space Agency, the Research Council of Finland, the Romanian Space Agency, the State Secretariat for Education, Research, and Innovation (SERI) at the Swiss Space Office (SSO), and the United Kingdom Space Agency. A complete and detailed list is available on the *Euclid* web site ([www.euclid-ec.org](http://www.euclid-ec.org)). This work has made use of the *Euclid* Quick Release Q1 data from the *Euclid* mission of the European Space Agency (ESA), 2025, <https://doi.org/10.57780/esa-2853f3b>. This research makes use of ESA Datalabs ([datalabs.esa.int](https://datalabs.esa.int)), an initiative by ESA’s Data Science and Archives Division in the Science and Operations Department, Directorate of Science.

## References

Acevedo Barroso, J. A., Clément, B., Courbin, F., et al. 2024a, in IAU Symposium, ed. H. Stacey, A. Sonnenfeld, & C. Grillo, Vol. 381, 17–22  
 Acevedo Barroso, J. A., O’Riordan, C. M., Clément, B., et al. 2024b, arXiv e-prints, arXiv:2408.06217  
 Avestruz, C., Li, N., Zhu, H., et al. 2019, ApJ, 877, 58

Birrer, S. & Amara, A. 2018, Physics of the Dark Universe, 22, 189  
 Birrer, S., Shajib, A. J., Gilman, D., et al. 2021, Journal of Open Source Software, 6, 3283  
 Cañameras, R., Schuldt, S., Shu, Y., et al. 2024, A&A, 692, A72  
 Cañameras, R., Schuldt, S., Suyu, S. H., et al. 2020, A&A, 644, A163  
 Collett, T. E. 2015, ApJ, 811, 20  
 Collett, T. E. & Bacon, D. J. 2016, MNRAS, 456, 2210  
 Collett, T. E., Oldham, L. J., Smith, R. J., et al. 2018, Science, 360, 1342  
 Domínguez Sánchez, H., Huertas-Company, M., Bernardi, M., Tuccillo, D., & Fischer, J. L. 2018, MNRAS, 476, 3661  
 Dux, F., Millon, M., Lemon, C., et al. 2024, arXiv:2411.04177  
 Euclid Collaboration: Castander, F., Fosalba, P., Stadel, J., et al. 2024, A&A, accepted, arXiv:2405.13495  
 Euclid Collaboration: Cropper, M., Al Bahlawan, A., Amiaux, J., et al. 2024, A&A, accepted, arXiv:2405.13492  
 Euclid Collaboration: Holloway, P., Verma, A., Walmsley, M., et al. 2025, A&A, submitted  
 Euclid Collaboration: Jahnke, K., Gillard, W., Schirmer, M., et al. 2024, A&A, accepted, arXiv:2405.13493  
 Euclid Collaboration: Leuzzi, L., Meneghetti, M., Angora, G., et al. 2024, A&A, 681, A68  
 Euclid Collaboration: Li, T., Collett, T., Walmsley, M., et al. 2025, A&A, submitted  
 Euclid Collaboration: McCracken, H., Benson, K., et al. 2025, A&A, submitted  
 Euclid Collaboration: Mellier, Y., Abdurro’uf, Acevedo Barroso, J. A., et al. 2024, arXiv e-prints, arXiv:2405.13491  
 Euclid Collaboration: Rojas, K., Collett, T., Acevedo Barroso, J., et al. 2025, A&A, submitted  
 Euclid Collaboration: Romelli, E., Kümmel, M., Dole, H., et al. 2025, A&A, submitted  
 Euclid Collaboration: Scaramella, R., Amiaux, J., Mellier, Y., et al. 2022, A&A, 662, A112  
 Euclid Collaboration: Walmsley, M., Holloway, P., Lines, N., et al. 2025, A&A, submitted  
 Euclid Early Release Observations. 2024, <https://doi.org/10.57780/esa-qmocz3>  
 Euclid Quick Release Q1. 2025, <https://doi.org/10.57780/esa-2853f3b>  
 González, J., Holloway, P., Collett, T., et al. 2025, arXiv e-prints, arXiv:2501.15679  
 Grespan, M., Thuruthipilly, H., Pollo, A., et al. 2024, A&A, 688, A34  
 Harvey-Hawes, C. & Galoppo, M. 2024, arXiv e-prints, arXiv:2411.17888  
 Jacobs, C., Collett, T., Glazebrook, K., et al. 2019a, ApJS, 243, 17  
 Jacobs, C., Collett, T., Glazebrook, K., et al. 2019b, MNRAS, 484, 5330  
 Jacobs, C., Glazebrook, K., Collett, T., More, A., & McCarthy, C. 2017, MNRAS, 471, 167  
 Jaelani, A. T., More, A., Wong, K. C., et al. 2024, MNRAS, 535, 1625  
 Kingma, D. P. & Ba, J. L. 2015, in International Conference on Learning Representations  
 Koekemoer, A. M., Aussel, H., Calzetti, D., et al. 2007, ApJS, 172, 196  
 Lanusse, F., Ma, Q., Li, N., et al. 2018, MNRAS, 473, 3895  
 Leauthaud, A., Massey, R., Kneib, J.-P., et al. 2007, ApJS, 172, 219  
 Li, R., Napolitano, N. R., Spiniello, C., et al. 2021, ApJ, 923, 16  
 Li, R., Napolitano, N. R., Tortora, C., et al. 2020, ApJ, 899, 30  
 Lintott, C. J., Schawinski, K., Slosar, A., et al. 2008, MNRAS, 389, 1179  
 Liu, Z., Mao, H., Wu, C.-Y., et al. 2022, arXiv e-prints, arXiv:2201.03545  
 Manjón-García, A. 2021, Phd thesis, University of Cantabria (Spain)  
 Marshall, P. J., Verma, A., More, A., et al. 2015, MNRAS, 455, 1171  
 Metcalf, R. B., Meneghetti, M., Avestruz, C., et al. 2019, A&A, 625, A119  
 Metcalf, R. B. & Petkova, M. 2014, MNRAS, 445, 1942  
 More, A., Verma, A., Marshall, P. J., et al. 2016, MNRAS, 455, 1191  
 Nagam, B. C., Acevedo Barroso, J. A., Wilde, J., et al. 2025, A&A, submitted, arXiv:2502.09802  
 Nagam, B. C., Koopmans, L. V. E., Valentijn, E. A., et al. 2023, MNRAS, 523, 4188  
 Nagam, B. C., Koopmans, L. V. E., Valentijn, E. A., et al. 2024, MNRAS, 533, 1426  
 Navarro, J. F., Frenk, C. S., & White, S. D. M. 1997, ApJ, 490, 493  
 O’Riordan, C. M., Oldham, L. J., Nersesian, A., et al. 2025, A&A, 694, A145  
 Pearce-Casey, R., Nagam, B. C., Wilde, J., et al. 2024, A&A, submitted, arXiv:2411.16808  
 Petkova, M., Metcalf, R. B., & Giocoli, C. 2014, MNRAS, 445, 1954  
 Petrillo, C. E., Tortora, C., Chatterjee, S., et al. 2017, MNRAS, 472, 1129  
 Petrillo, C. E., Tortora, C., Vernardos, G., et al. 2019, MNRAS, 484, 3879  
 Rojas, K., Collett, T. E., Ballard, D., et al. 2023, MNRAS, 523, 4413  
 Rojas, K., Savary, E., Clément, B., et al. 2022, A&A, 668, A73  
 Savary, E., Rojas, K., Maus, M., et al. 2022, A&A, 666, A1  
 Schuldt, S., Suyu, S. H., Meinhardt, T., et al. 2021, A&A, 646, A126  
 Scoville, N., Aussel, H., Brusa, M., et al. 2007, ApJS, 172, 1  
 Shu, Y., Cañameras, R., Schuldt, S., et al. 2022, A&A, 662, A4  
 Sonnenfeld, A., Verma, A., More, A., et al. 2020, A&A, 642, A148

- Suyu, S. H. & Halkola, A. 2010, *A&A*, 524, A94
- Suyu, S. H., Hensel, S. W., McKean, J. P., et al. 2012, *ApJ*, 750, 10
- Szegedy, C., Liu, W., Jia, Y., et al. 2014, arXiv e-prints, arXiv:1409.4842
- Szegedy, C., Vanhoucke, V., Ioffe, S., Shlens, J., & Wojna, Z. 2015, arXiv e-prints, arXiv:1512.00567
- Tortora, C., Posti, L., Koopmans, L. V. E., & Napolitano, N. R. 2019, *MNRAS*, 489, 5483
- Treu, T., Dutton, A. A., Auger, M. W., et al. 2011, *MNRAS*, 417, 1601
- Walmsley, M., Allen, C., Aussel, B., et al. 2023, *Journal of Open Source Software*, 8, 5312
- Walmsley, M., Bowles, M., Scaife, A. M. M., et al. 2024, arXiv e-prints, arXiv:2404.02973
- Weaver, J. R., Kauffmann, O. B., Ilbert, O., et al. 2022, *ApJS*, 258, 11
- Wilde, J., Serjeant, S., Bromley, J. M., et al. 2022, *MNRAS*, 512, 3464
- 27 Max-Planck-Institut für Astronomie, Königstuhl 17, 69117 Heidelberg, Germany
- 28 ESAC/ESA, Camino Bajo del Castillo, s/n., Urb. Villafranca del Castillo, 28692 Villanueva de la Cañada, Madrid, Spain
- 29 STAR Institute, University of Liège, Quartier Agora, Allée du six Août 19c, 4000 Liège, Belgium
- 30 Department of Physics, Centre for Extragalactic Astronomy, Durham University, South Road, Durham, DH1 3LE, UK
- 31 Department of Physics, Institute for Computational Cosmology, Durham University, South Road, Durham, DH1 3LE, UK
- 32 The Inter-University Centre for Astronomy and Astrophysics, Post Bag 4, Ganeshkhind, Pune 411007, India
- 33 Kavli Institute for the Physics and Mathematics of the Universe (WPI), University of Tokyo, Kashiwa, Chiba 277-8583, Japan
- 34 Minnesota Institute for Astrophysics, University of Minnesota, 116 Church St SE, Minneapolis, MN 55455, USA
- 35 Kapteyn Astronomical Institute, University of Groningen, PO Box 800, 9700 AV Groningen, The Netherlands
- 36 Department of Astronomy, School of Physics and Astronomy, Shanghai Jiao Tong University, Shanghai 200240, China
- 37 National Astronomical Observatory of Japan, 2-21-1 Osawa, Mitaka, Tokyo 181-8588, Japan
- 38 INAF-Osservatorio Astronomico di Capodimonte, Via Moiariello 16, 80131 Napoli, Italy
- 39 University of Trento, Via Sommarive 14, I-38123 Trento, Italy
- 40 Dipartimento di Fisica e Astronomia, Università di Firenze, via G. Sansone 1, 50019 Sesto Fiorentino, Firenze, Italy
- 41 INAF-Osservatorio Astrofisico di Arcetri, Largo E. Fermi 5, 50125, Firenze, Italy
- 42 Max Planck Institute for Gravitational Physics (Albert Einstein Institute), Am Mühlenberg 1, D-14476 Potsdam-Golm, Germany
- 43 Université Paris-Saclay, CNRS, Institut d'astrophysique spatiale, 91405, Orsay, France
- 44 School of Mathematics and Physics, University of Surrey, Guildford, Surrey, GU2 7XH, UK
- 45 INAF-Osservatorio Astronomico di Brera, Via Brera 28, 20122 Milano, Italy
- 46 Université Paris-Saclay, Université Paris Cité, CEA, CNRS, AIM, 91191, Gif-sur-Yvette, France
- 47 IFPU, Institute for Fundamental Physics of the Universe, via Beirut 2, 34151 Trieste, Italy
- 48 INAF-Osservatorio Astronomico di Trieste, Via G. B. Tiepolo 11, 34143 Trieste, Italy
- 49 INFN, Sezione di Trieste, Via Valerio 2, 34127 Trieste TS, Italy
- 50 SISSA, International School for Advanced Studies, Via Bonomea 265, 34136 Trieste TS, Italy
- 51 Dipartimento di Fisica e Astronomia, Università di Bologna, Via Gobetti 93/2, 40129 Bologna, Italy
- 52 INAF-Osservatorio Astronomico di Padova, Via dell'Osservatorio 5, 35122 Padova, Italy
- 53 Institut de Physique Théorique, CEA, CNRS, Université Paris-Saclay 91191 Gif-sur-Yvette Cedex, France
- 54 Space Science Data Center, Italian Space Agency, via del Politecnico snc, 00133 Roma, Italy
- 55 INAF-Osservatorio Astrofisico di Torino, Via Osservatorio 20, 10025 Pino Torinese (TO), Italy
- 56 Dipartimento di Fisica, Università di Genova, Via Dodecaneso 33, 16146, Genova, Italy
- 57 INFN-Sezione di Genova, Via Dodecaneso 33, 16146, Genova, Italy
- 58 Department of Physics "E. Pancini", University Federico II, Via Cinthia 6, 80126, Napoli, Italy
- 59 Instituto de Astrofísica e Ciências do Espaço, Universidade do Porto, CAUP, Rua das Estrelas, PT4150-762 Porto, Portugal
- 60 Faculdade de Ciências da Universidade do Porto, Rua do Campo de Alegre, 4150-007 Porto, Portugal
- 61 Dipartimento di Fisica, Università degli Studi di Torino, Via P. Giuria 1, 10125 Torino, Italy
- 62 INFN-Sezione di Torino, Via P. Giuria 1, 10125 Torino, Italy
- 
- 1 Institute of Cosmology and Gravitation, University of Portsmouth, Portsmouth PO1 3FX, UK
- 2 David A. Dunlap Department of Astronomy & Astrophysics, University of Toronto, 50 St George Street, Toronto, Ontario M5S 3H4, Canada
- 3 Jodrell Bank Centre for Astrophysics, Department of Physics and Astronomy, University of Manchester, Oxford Road, Manchester M13 9PL, UK
- 4 University of Applied Sciences and Arts of Northwestern Switzerland, School of Engineering, 5210 Windisch, Switzerland
- 5 Dipartimento di Fisica e Astronomia "Augusto Righi" - Alma Mater Studiorum Università di Bologna, via Piero Gobetti 93/2, 40129 Bologna, Italy
- 6 INAF-Osservatorio di Astrofisica e Scienza dello Spazio di Bologna, Via Piero Gobetti 93/3, 40129 Bologna, Italy
- 7 Departamento Física Aplicada, Universidad Politécnica de Cartagena, Campus Muralla del Mar, 30202 Cartagena, Murcia, Spain
- 8 Institut de Ciències del Cosmos (ICCUB), Universitat de Barcelona (IEEC-UB), Martí i Franquès 1, 08028 Barcelona, Spain
- 9 Department of Physics, Oxford University, Keble Road, Oxford OX1 3RH, UK
- 10 Technical University of Munich, TUM School of Natural Sciences, Physics Department, James-Frank-Str. 1, 85748 Garching, Germany
- 11 Max-Planck-Institut für Astrophysik, Karl-Schwarzschild-Str. 1, 85748 Garching, Germany
- 12 Instituto de Física de Cantabria, Edificio Juan Jordá, Avenida de los Castros, 39005 Santander, Spain
- 13 Institute of Physics, Laboratory of Astrophysics, Ecole Polytechnique Fédérale de Lausanne (EPFL), Observatoire de Sauverny, 1290 Versoix, Switzerland
- 14 SCITAS, Ecole Polytechnique Fédérale de Lausanne (EPFL), 1015 Lausanne, Switzerland
- 15 School of Physical Sciences, The Open University, Milton Keynes, MK7 6AA, UK
- 16 Institució Catalana de Recerca i Estudis Avançats (ICREA), Pas-seig de Luís Companys 23, 08010 Barcelona, Spain
- 17 INFN-Sezione di Bologna, Viale Bertini Pichat 6/2, 40127 Bologna, Italy
- 18 Aix-Marseille Université, CNRS, CNES, LAM, Marseille, France
- 19 Institut d'Astrophysique de Paris, UMR 7095, CNRS, and Sorbonne Université, 98 bis boulevard Arago, 75014 Paris, France
- 20 Dipartimento di Fisica "Aldo Pontremoli", Università degli Studi di Milano, Via Celoria 16, 20133 Milano, Italy
- 21 INAF-IASF Milano, Via Alfonso Corti 12, 20133 Milano, Italy
- 22 Department of Astronomy, University of Geneva, ch. d'Ecogia 16, 1290 Versoix, Switzerland
- 23 Universitäts-Sternwarte München, Fakultät für Physik, Ludwig-Maximilians-Universität München, Scheinerstrasse 1, 81679 München, Germany
- 24 Max Planck Institute for Extraterrestrial Physics, Giessenbachstr. 1, 85748 Garching, Germany
- 25 Caltech/IPAC, 1200 E. California Blvd., Pasadena, CA 91125, USA
- 26 Laboratoire univers et particules de Montpellier, Université de Montpellier, CNRS, 34090 Montpellier, France

- <sup>63</sup> European Space Agency/ESTEC, Keplerlaan 1, 2201 AZ Noordwijk, The Netherlands
- <sup>64</sup> Institute Lorentz, Leiden University, Niels Bohrweg 2, 2333 CA Leiden, The Netherlands
- <sup>65</sup> Leiden Observatory, Leiden University, Einsteinweg 55, 2333 CC Leiden, The Netherlands
- <sup>66</sup> INAF-Osservatorio Astronomico di Roma, Via Frascati 33, 00078 Monteporzio Catone, Italy
- <sup>67</sup> INFN-Sezione di Roma, Piazzale Aldo Moro, 2 - c/o Dipartimento di Fisica, Edificio G. Marconi, 00185 Roma, Italy
- <sup>68</sup> Centro de Investigaciones Energéticas, Medioambientales y Tecnológicas (CIEMAT), Avenida Complutense 40, 28040 Madrid, Spain
- <sup>69</sup> Port d'Informació Científica, Campus UAB, C. Albareda s/n, 08193 Bellaterra (Barcelona), Spain
- <sup>70</sup> Institute for Theoretical Particle Physics and Cosmology (TTK), RWTH Aachen University, 52056 Aachen, Germany
- <sup>71</sup> INFN section of Naples, Via Cinthia 6, 80126, Napoli, Italy
- <sup>72</sup> Institute for Astronomy, University of Hawaii, 2680 Woodlawn Drive, Honolulu, HI 96822, USA
- <sup>73</sup> Dipartimento di Fisica e Astronomia "Augusto Righi" - Alma Mater Studiorum Università di Bologna, Viale Bertini Pichat 6/2, 40127 Bologna, Italy
- <sup>74</sup> Instituto de Astrofísica de Canarias, Vía Láctea, 38205 La Laguna, Tenerife, Spain
- <sup>75</sup> Institute for Astronomy, University of Edinburgh, Royal Observatory, Blackford Hill, Edinburgh EH9 3HJ, UK
- <sup>76</sup> European Space Agency/ESRIN, Largo Galileo Galilei 1, 00044 Frascati, Roma, Italy
- <sup>77</sup> Université Claude Bernard Lyon 1, CNRS/IN2P3, IP2I Lyon, UMR 5822, Villeurbanne, F-69100, France
- <sup>78</sup> UCB Lyon 1, CNRS/IN2P3, IUF, IP2I Lyon, 4 rue Enrico Fermi, 69622 Villeurbanne, France
- <sup>79</sup> Mullard Space Science Laboratory, University College London, Holmbury St Mary, Dorking, Surrey RH5 6NT, UK
- <sup>80</sup> Departamento de Física, Faculdade de Ciências, Universidade de Lisboa, Edifício C8, Campo Grande, PT1749-016 Lisboa, Portugal
- <sup>81</sup> Instituto de Astrofísica e Ciências do Espaço, Faculdade de Ciências, Universidade de Lisboa, Campo Grande, 1749-016 Lisboa, Portugal
- <sup>82</sup> INAF-Istituto di Astrofisica e Planetologia Spaziali, via del Cavaliere, 100, 00100 Roma, Italy
- <sup>83</sup> Aix-Marseille Université, CNRS/IN2P3, CPPM, Marseille, France
- <sup>84</sup> INFN-Bologna, Via Irnerio 46, 40126 Bologna, Italy
- <sup>85</sup> School of Physics, HH Wills Physics Laboratory, University of Bristol, Tyndall Avenue, Bristol, BS8 1TL, UK
- <sup>86</sup> FRACTAL S.L.N.E., calle Tulipán 2, Portal 13 1A, 28231, Las Rozas de Madrid, Spain
- <sup>87</sup> INFN-Sezione di Milano, Via Celoria 16, 20133 Milano, Italy
- <sup>88</sup> NRC Herzberg, 5071 West Saanich Rd, Victoria, BC V9E 2E7, Canada
- <sup>89</sup> Institute of Theoretical Astrophysics, University of Oslo, P.O. Box 1029 Blindern, 0315 Oslo, Norway
- <sup>90</sup> Jet Propulsion Laboratory, California Institute of Technology, 4800 Oak Grove Drive, Pasadena, CA, 91109, USA
- <sup>91</sup> Department of Physics, Lancaster University, Lancaster, LA1 4YB, UK
- <sup>92</sup> Felix Hormuth Engineering, Goethestr. 17, 69181 Leimen, Germany
- <sup>93</sup> Technical University of Denmark, Elektrovej 327, 2800 Kgs. Lyngby, Denmark
- <sup>94</sup> Cosmic Dawn Center (DAWN), Denmark
- <sup>95</sup> NASA Goddard Space Flight Center, Greenbelt, MD 20771, USA
- <sup>96</sup> Department of Physics and Helsinki Institute of Physics, Gustaf Hällströmin katu 2, 00014 University of Helsinki, Finland
- <sup>97</sup> Université de Genève, Département de Physique Théorique and Centre for Astroparticle Physics, 24 quai Ernest-Ansermet, CH-1211 Genève 4, Switzerland
- <sup>98</sup> Department of Physics, P.O. Box 64, 00014 University of Helsinki, Finland
- <sup>99</sup> Helsinki Institute of Physics, Gustaf Hällströmin katu 2, University of Helsinki, Helsinki, Finland
- <sup>100</sup> Centre de Calcul de l'IN2P3/CNRS, 21 avenue Pierre de Coubertin 69627 Villeurbanne Cedex, France
- <sup>101</sup> Laboratoire d'étude de l'Univers et des phénomènes eXtremes, Observatoire de Paris, Université PSL, Sorbonne Université, CNRS, 92190 Meudon, France
- <sup>102</sup> SKA Observatory, Jodrell Bank, Lower Withington, Macclesfield, Cheshire SK11 9FT, UK
- <sup>103</sup> University of Applied Sciences and Arts of Northwestern Switzerland, School of Computer Science, 5210 Windisch, Switzerland
- <sup>104</sup> Universität Bonn, Argelander-Institut für Astronomie, Auf dem Hügel 71, 53121 Bonn, Germany
- <sup>105</sup> Université Côte d'Azur, Observatoire de la Côte d'Azur, CNRS, Laboratoire Lagrange, Bd de l'Observatoire, CS 34229, 06304 Nice cedex 4, France
- <sup>106</sup> Université Paris Cité, CNRS, Astroparticule et Cosmologie, 75013 Paris, France
- <sup>107</sup> CNRS-UCB International Research Laboratory, Centre Pierre Binetruy, IRL2007, CPB-IN2P3, Berkeley, USA
- <sup>108</sup> Institut d'Astrophysique de Paris, 98bis Boulevard Arago, 75014, Paris, France
- <sup>109</sup> Aurora Technology for European Space Agency (ESA), Camino bajo del Castillo, s/n, Urbanización Villafranca del Castillo, Villanueva de la Cañada, 28692 Madrid, Spain
- <sup>110</sup> Institut de Física d'Altes Energies (IFAE), The Barcelona Institute of Science and Technology, Campus UAB, 08193 Bellaterra (Barcelona), Spain
- <sup>111</sup> School of Mathematics, Statistics and Physics, Newcastle University, Herschel Building, Newcastle-upon-Tyne, NE1 7RU, UK
- <sup>112</sup> DARK, Niels Bohr Institute, University of Copenhagen, Jagtvej 155, 2200 Copenhagen, Denmark
- <sup>113</sup> Waterloo Centre for Astrophysics, University of Waterloo, Waterloo, Ontario N2L 3G1, Canada
- <sup>114</sup> Department of Physics and Astronomy, University of Waterloo, Waterloo, Ontario N2L 3G1, Canada
- <sup>115</sup> Perimeter Institute for Theoretical Physics, Waterloo, Ontario N2L 2Y5, Canada
- <sup>116</sup> Centre National d'Etudes Spatiales – Centre spatial de Toulouse, 18 avenue Edouard Belin, 31401 Toulouse Cedex 9, France
- <sup>117</sup> Institute of Space Science, Str. Atomistilor, nr. 409 Măgurele, Ilfov, 077125, Romania
- <sup>118</sup> Consejo Superior de Investigaciones Científicas, Calle Serrano 117, 28006 Madrid, Spain
- <sup>119</sup> Universidad de La Laguna, Departamento de Astrofísica, 38206 La Laguna, Tenerife, Spain
- <sup>120</sup> Dipartimento di Fisica e Astronomia "G. Galilei", Università di Padova, Via Marzolo 8, 35131 Padova, Italy
- <sup>121</sup> INFN-Padova, Via Marzolo 8, 35131 Padova, Italy
- <sup>122</sup> Institut für Theoretische Physik, University of Heidelberg, Philosophenweg 16, 69120 Heidelberg, Germany
- <sup>123</sup> Institut de Recherche en Astrophysique et Planétologie (IRAP), Université de Toulouse, CNRS, UPS, CNES, 14 Av. Edouard Belin, 31400 Toulouse, France
- <sup>124</sup> Université St Joseph; Faculty of Sciences, Beirut, Lebanon
- <sup>125</sup> Departamento de Física, FCFM, Universidad de Chile, Blanco Encalada 2008, Santiago, Chile
- <sup>126</sup> Universität Innsbruck, Institut für Astro- und Teilchenphysik, Technikerstr. 25/8, 6020 Innsbruck, Austria
- <sup>127</sup> Institut d'Estudis Espacials de Catalunya (IEEC), Edifici RDIT, Campus UPC, 08860 Castelldefels, Barcelona, Spain
- <sup>128</sup> Atlantis, University Science Park, Sede Bld 48940, Leioa-Bilbao, Spain
- <sup>129</sup> Institute of Space Sciences (ICE, CSIC), Campus UAB, Carrer de Can Magrans, s/n, 08193 Barcelona, Spain
- <sup>130</sup> Department of Physics, Royal Holloway, University of London, TW20 0EX, UK
- <sup>131</sup> Instituto de Astrofísica e Ciências do Espaço, Faculdade de Ciências, Universidade de Lisboa, Tapada da Ajuda, 1349-018 Lisboa, Portugal

- <sup>132</sup> Cosmic Dawn Center (DAWN)  
<sup>133</sup> Niels Bohr Institute, University of Copenhagen, Jagtvej 128, 2200 Copenhagen, Denmark  
<sup>134</sup> Universidad Politécnica de Cartagena, Departamento de Electrónica y Tecnología de Computadoras, Plaza del Hospital 1, 30202 Cartagena, Spain  
<sup>135</sup> Infrared Processing and Analysis Center, California Institute of Technology, Pasadena, CA 91125, USA  
<sup>136</sup> Dipartimento di Fisica e Scienze della Terra, Università degli Studi di Ferrara, Via Giuseppe Saragat 1, 44122 Ferrara, Italy  
<sup>137</sup> Istituto Nazionale di Fisica Nucleare, Sezione di Ferrara, Via Giuseppe Saragat 1, 44122 Ferrara, Italy  
<sup>138</sup> INAF, Istituto di Radioastronomia, Via Piero Gobetti 101, 40129 Bologna, Italy  
<sup>139</sup> INAF - Osservatorio Astronomico di Brera, via Emilio Bianchi 46, 23807 Merate, Italy  
<sup>140</sup> INAF-Osservatorio Astronomico di Brera, Via Brera 28, 20122 Milano, Italy, and INFN-Sezione di Genova, Via Dodecaneso 33, 16146, Genova, Italy  
<sup>141</sup> ICL, Junia, Université Catholique de Lille, LITL, 59000 Lille, France  
<sup>142</sup> ICSC - Centro Nazionale di Ricerca in High Performance Computing, Big Data e Quantum Computing, Via Magnanelli 2, Bologna, Italy  
<sup>143</sup> Instituto de Física Teórica UAM-CSIC, Campus de Cantoblanco, 28049 Madrid, Spain  
<sup>144</sup> CERCA/ISO, Department of Physics, Case Western Reserve University, 10900 Euclid Avenue, Cleveland, OH 44106, USA  
<sup>145</sup> Laboratoire Univers et Théorie, Observatoire de Paris, Université PSL, Université Paris Cité, CNRS, 92190 Meudon, France  
<sup>146</sup> Departamento de Física Fundamental, Universidad de Salamanca, Plaza de la Merced s/n. 37008 Salamanca, Spain  
<sup>147</sup> Université de Strasbourg, CNRS, Observatoire astronomique de Strasbourg, UMR 7550, 67000 Strasbourg, France  
<sup>148</sup> Center for Data-Driven Discovery, Kavli IPMU (WPI), UTIAS, The University of Tokyo, Kashiwa, Chiba 277-8583, Japan  
<sup>149</sup> California Institute of Technology, 1200 E California Blvd, Pasadena, CA 91125, USA  
<sup>150</sup> Department of Physics & Astronomy, University of California Irvine, Irvine CA 92697, USA  
<sup>151</sup> Department of Mathematics and Physics E. De Giorgi, University of Salento, Via per Arnesano, CP-193, 73100, Lecce, Italy  
<sup>152</sup> INFN, Sezione di Lecce, Via per Arnesano, CP-193, 73100, Lecce, Italy  
<sup>153</sup> INAF-Sezione di Lecce, c/o Dipartimento Matematica e Fisica, Via per Arnesano, 73100, Lecce, Italy  
<sup>154</sup> Instituto de Astrofísica de Canarias (IAC); Departamento de Astrofísica, Universidad de La Laguna (ULL), 38200, La Laguna, Tenerife, Spain  
<sup>155</sup> CEA Saclay, DFR/IRFU, Service d'Astrophysique, Bat. 709, 91191 Gif-sur-Yvette, France  
<sup>156</sup> Department of Computer Science, Aalto University, PO Box 15400, Espoo, FI-00 076, Finland  
<sup>157</sup> Instituto de Astrofísica de Canarias, c/ Via Lactea s/n, La Laguna 38200, Spain. Departamento de Astrofísica de la Universidad de La Laguna, Avda. Francisco Sanchez, La Laguna, 38200, Spain  
<sup>158</sup> Ruhr University Bochum, Faculty of Physics and Astronomy, Astronomical Institute (AIRUB), German Centre for Cosmological Lensing (GCCL), 44780 Bochum, Germany  
<sup>159</sup> Department of Physics and Astronomy, Vesilinnantie 5, 20014 University of Turku, Finland  
<sup>160</sup> Serco for European Space Agency (ESA), Camino bajo del Castillo, s/n, Urbanización Villafranca del Castillo, Villanueva de la Cañada, 28692 Madrid, Spain  
<sup>161</sup> ARC Centre of Excellence for Dark Matter Particle Physics, Melbourne, Australia  
<sup>162</sup> Centre for Astrophysics & Supercomputing, Swinburne University of Technology, Hawthorn, Victoria 3122, Australia  
<sup>163</sup> Department of Physics and Astronomy, University of the Western Cape, Bellville, Cape Town, 7535, South Africa  
<sup>164</sup> DAMTP, Centre for Mathematical Sciences, Wilberforce Road, Cambridge CB3 0WA, UK  
<sup>165</sup> Kavli Institute for Cosmology Cambridge, Madingley Road, Cambridge, CB3 0HA, UK  
<sup>166</sup> Department of Astrophysics, University of Zurich, Winterthurerstrasse 190, 8057 Zurich, Switzerland  
<sup>167</sup> IRFU, CEA, Université Paris-Saclay 91191 Gif-sur-Yvette Cedex, France  
<sup>168</sup> Oskar Klein Centre for Cosmoparticle Physics, Department of Physics, Stockholm University, Stockholm, SE-106 91, Sweden  
<sup>169</sup> Astrophysics Group, Blackett Laboratory, Imperial College London, London SW7 2AZ, UK  
<sup>170</sup> Univ. Grenoble Alpes, CNRS, Grenoble INP, LPSC-IN2P3, 53, Avenue des Martyrs, 38000, Grenoble, France  
<sup>171</sup> Dipartimento di Fisica, Sapienza Università di Roma, Piazzale Aldo Moro 2, 00185 Roma, Italy  
<sup>172</sup> Centro de Astrofísica da Universidade do Porto, Rua das Estrelas, 4150-762 Porto, Portugal  
<sup>173</sup> HE Space for European Space Agency (ESA), Camino bajo del Castillo, s/n, Urbanización Villafranca del Castillo, Villanueva de la Cañada, 28692 Madrid, Spain  
<sup>174</sup> Dipartimento di Fisica - Sezione di Astronomia, Università di Trieste, Via Tiepolo 11, 34131 Trieste, Italy  
<sup>175</sup> Department of Astrophysical Sciences, Peyton Hall, Princeton University, Princeton, NJ 08544, USA  
<sup>176</sup> Theoretical astrophysics, Department of Physics and Astronomy, Uppsala University, Box 515, 751 20 Uppsala, Sweden  
<sup>177</sup> Mathematical Institute, University of Leiden, Einsteinweg 55, 2333 CA Leiden, The Netherlands  
<sup>178</sup> Institute of Astronomy, University of Cambridge, Madingley Road, Cambridge CB3 0HA, UK  
<sup>179</sup> Space physics and astronomy research unit, University of Oulu, Pentti Kaiteran katu 1, FI-90014 Oulu, Finland  
<sup>180</sup> Department of Physics and Astronomy, Lehman College of the CUNY, Bronx, NY 10468, USA  
<sup>181</sup> American Museum of Natural History, Department of Astrophysics, New York, NY 10024, USA  
<sup>182</sup> Center for Computational Astrophysics, Flatiron Institute, 162 5th Avenue, 10010, New York, NY, USA  
<sup>183</sup> Department of Physics and Astronomy, University of British Columbia, Vancouver, BC V6T 1Z1, Canada

**Appendix A: Images of lenses discovered***Appendix A.1: Top grade A candidates*

In Fig. A.1 we show the top 56/250 grade A lenses, ranked according to GJ score assigned during expert visual inspection.



**Fig. A.1.** The top 56/250 grade A lenses discovered in Q1, ranked (left to right, top to bottom) by GJ expert inspection score.

## Appendix A.2: DSPLs

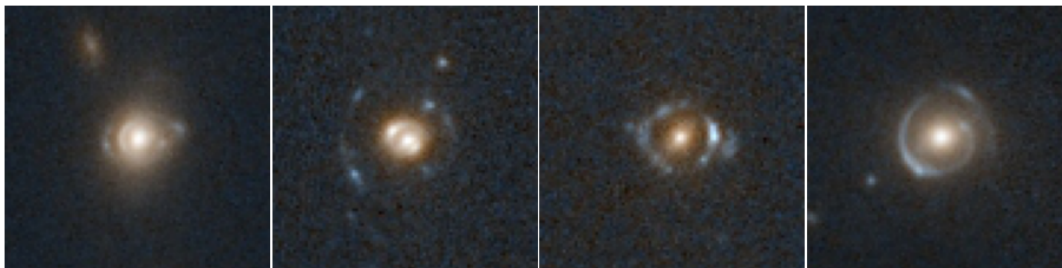


**Fig. A.2.** The four confirmed DSPLs discovered in Q1. From left to right, they are the ‘teapot lens’, the ‘cosmic dartboard’, ‘Galileo’s lens’, and the ‘cosmic ammonite’.

In Fig. A.2 we show four DSPLs found in Q1 that have been successfully modelled as DSPLs by [Euclid Collaboration: Li et al. \(2025\)](#).

## Appendix A.3: Edge-on lenses



**Fig. A.3.** A selection of 42 of the grade A+B lenses where the lensing galaxy is an edge-on disc or lenticular galaxy. Because these lenses typically have smaller Einstein radii we use a smaller cutout size of  $70 \times 70$  pixels ( $7'' \times 7''$ ).

In Fig. A.3 we show grade A+B lenses discovered in Q1, where the lensing galaxy has a morphology closer to that of a disc or lenticular galaxy that is also at high inclination. Because the boundary between disc/lenticular/elliptical galaxies is not well defined, the 42 examples presented here should not be considered a complete list, but is included to display the diversity of lenses found in Q1.

## Appendix B: Example grade A/B/C lenses

In Fig. B.1 we show images ordered from most likely to least likely to be a lens according to expert inspection and the boundaries between grades A, B, and C to provide the reader with an understanding of what each grade refers to. For the full catalogue of lenses discovered we refer to [Euclid Collaboration: Walmsley et al. \(2025\)](#).

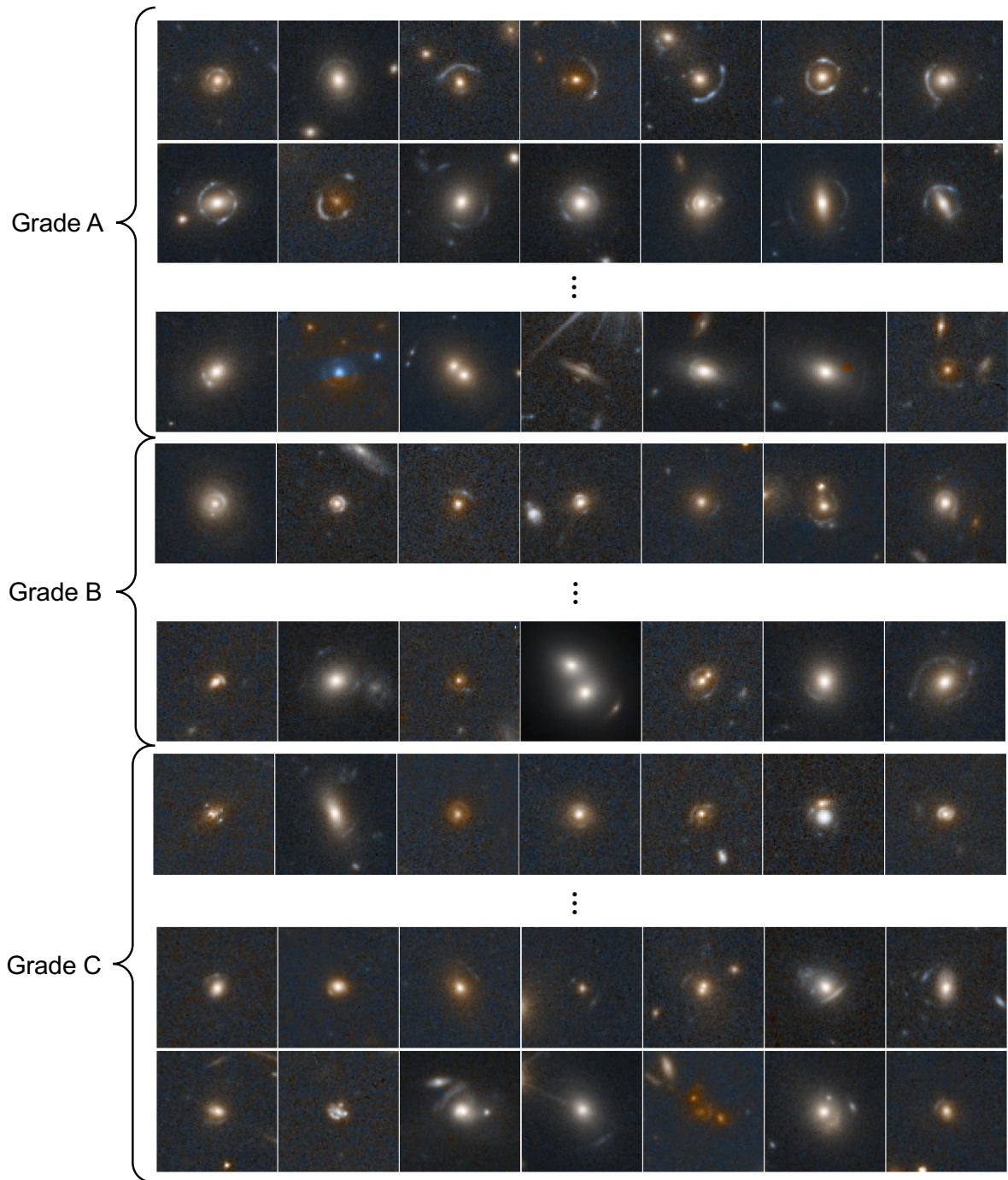


**Fig. B.1.** Images ranked by expert classification ordered from more likely to be a lens (top) to less likely to be a lens (bottom) at the upper and lower ends of the grade limits.

### Appendix C: Zoobot false positives

In Fig. C.1 we show the images that were ranked by Zoobot in the top 100 that were non-lenses according to expert inspection. Besides the two artefact images (ranked 65 and 79), the false positives can be loosely recognised as images containing multiple galaxies in close proximity, where one is typically more elongated. Although most of these are very obviously non-lenses, in many cases (e.g., images ranked 27, 39, 55, 70 etc.) it can at least be discerned what is being confused as an arc, and given the typical uninterpretability of CNNs, this is perhaps a good sign. Furthermore, if what is being confused as lenses are primarily serendipitous alignments of galaxies, these are much rarer than other typical false positives, such as spiral galaxies, and therefore this is less of a major concern. It is notable that in a minority of cases (e.g., image ranked 92) the more elongated galaxy is not centred on the other galaxy, showing that Zoobot is not necessarily learning any physical properties about the relationship between the lens and lensed galaxies. Reducing the prevalence of these false positives may be tricky; although the negative training set contained a ‘merger’ class that included images of multiple galaxies in different arrangements, the number of ways multiple galaxies can be oriented within one image is extremely large, so it is expected that some configurations could be confused with lensing systems. Additionally, the galaxies in these false positives are generally not very extended or well resolved, meaning they were unlikely to have been included in Zoobot’s pretraining on GalaxyZoo morphologies. However, as the quantity of *Euclid* data accumulates, we will be able to use known false positives from previous *Euclid* lens searches during the training for the next data releases, meaning we can hope for this to improve over time.

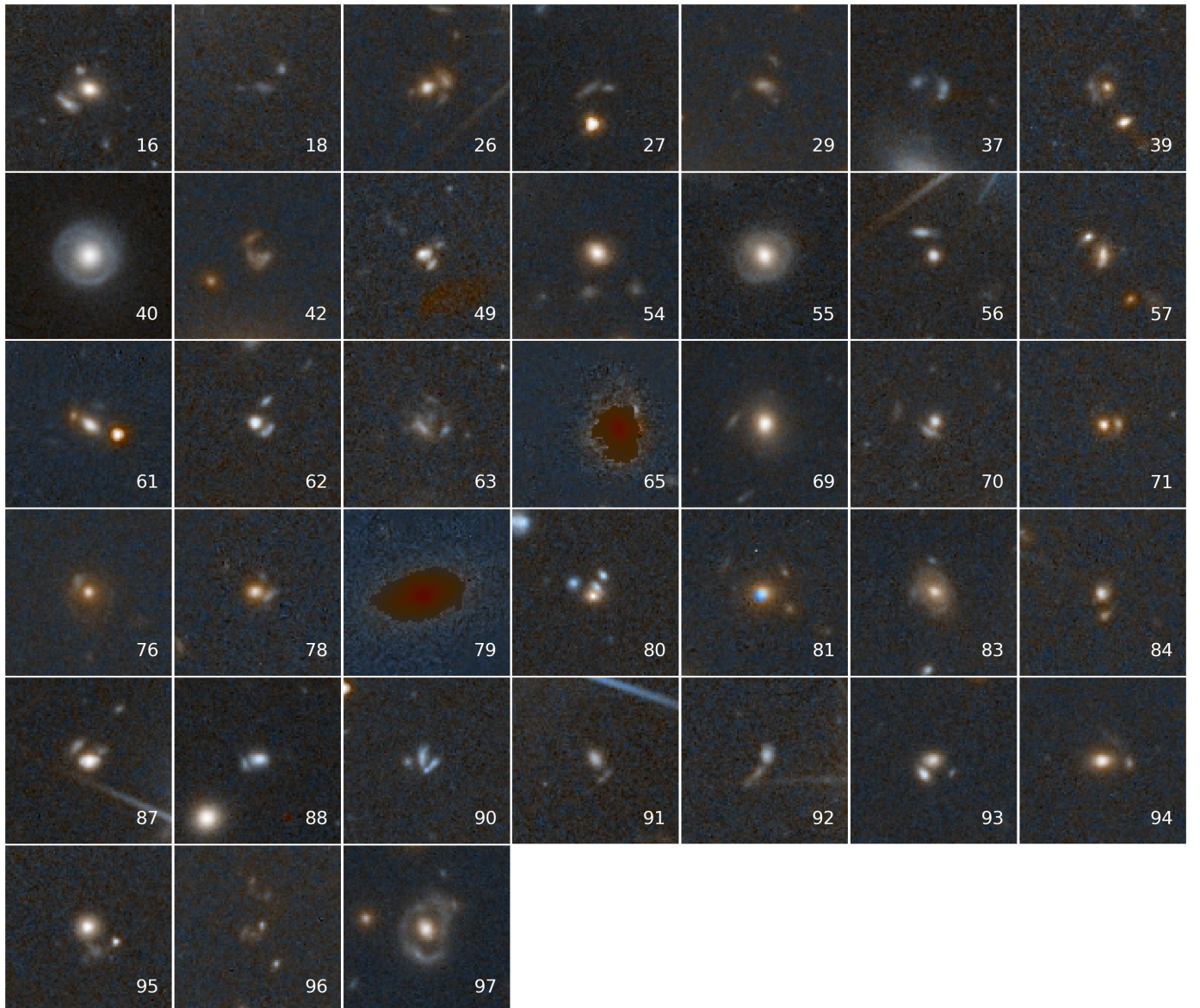


**Fig. C.1.** All the non-lenses that were ranked by Zoobot in the top 100 images. The number in each image displays how it was ranked by Zoobot.